



**HAL**  
open science

## Growth and global persistence of stratospheric sulfate aerosols from the 2022 Hunga Tonga-Hunga Haápai volcanic eruption

Marie Boichu, Raphaël Grandin, Luc Blarel, Benjamin Torres, Yevgeny Derimian, Philippe Goloub, Colette Brogniez, Isabelle Chiapello, O. Dubovik, Theo Mathurin, et al.

### ► To cite this version:

Marie Boichu, Raphaël Grandin, Luc Blarel, Benjamin Torres, Yevgeny Derimian, et al.. Growth and global persistence of stratospheric sulfate aerosols from the 2022 Hunga Tonga-Hunga Haápai volcanic eruption. *Journal of Geophysical Research: Atmospheres*, In press, 10.1029/2023JD039010 . hal-04272377

**HAL Id: hal-04272377**

**<https://hal.science/hal-04272377v1>**

Submitted on 6 Nov 2023

**HAL** is a multi-disciplinary open access archive for the deposit and dissemination of scientific research documents, whether they are published or not. The documents may come from teaching and research institutions in France or abroad, or from public or private research centers.

L'archive ouverte pluridisciplinaire **HAL**, est destinée au dépôt et à la diffusion de documents scientifiques de niveau recherche, publiés ou non, émanant des établissements d'enseignement et de recherche français ou étrangers, des laboratoires publics ou privés.



Distributed under a Creative Commons Attribution - NonCommercial 4.0 International License

1 **Growth and global persistence of stratospheric sulfate**  
2 **aerosols from the 2022 Hunga Tonga-Hunga Haápai**  
3 **volcanic eruption**

4 Marie Boichu<sup>1,2</sup>, Raphaél Grandin<sup>3</sup>, Luc Blarel<sup>1,2</sup>, Benjamin Torres<sup>2</sup>, Yevgeny  
5 Derimian<sup>1,2</sup>, Philippe Goloub<sup>2</sup>, Colette Brogniez<sup>2</sup>, Isabelle Chiapello<sup>1,2</sup>, Oleg  
6 Dubovik<sup>1,2</sup>, Théo Mathurin<sup>4</sup>, Nicolas Pascal<sup>1,4</sup>, Maximilien Patou<sup>4</sup>, Jérôme  
7 Riedi<sup>2,4</sup>

8 <sup>1</sup>CNRS, UMR 8518, F-59000 Lille, France

9 <sup>2</sup>University of Lille, UMR 8518 - LOA - Laboratoire d'Optique Atmosphérique, F-59000 Lille, France

10 <sup>3</sup>Université Paris Cité, Institut de Physique du Globe de Paris, CNRS, 75005 Paris, France

11 <sup>4</sup>University of Lille, CNRS, CNES, UMS 2877 – ICARE Data and Services Center, F-59000 Lille, France

12 **Key Points:**

- 13 • In the days following eruption, Hunga Tonga sulfate aerosols are observed to grow faster  
14 than Pinatubo particles.  
15 • Hunga Tonga stratospheric aerosols persist for >14 months as identified at 20 AERONET  
16 stations of the southern hemisphere.  
17 • One year after eruption, Hunga Tonga aerosols remain smaller than Pinatubo parti-  
18 cles, potentially implying an enhanced climate impact.

---

Corresponding author: Marie Boichu, [marie.boichu@univ-lille.fr](mailto:marie.boichu@univ-lille.fr)

**Abstract**

Stratospheric sulfate aerosols play a key role on atmospheric chemistry and Earth's radiation budget, but their size distribution, a critical parameter in climate models, is generally poorly-known. We address such gap for the 2022 Hunga Tonga-Hunga Haápai (HT-HH) volcanic eruption by exhaustively analyzing a set of satellite observations (TROPOMI, IASI, AHI, CALIOP) together with photometric ground observations from the worldwide open-access AERONET network. We document a rapid growth of HT-HH sulfate aerosols in the days following eruption, faster than observed for 1991 Pinatubo eruption, likely due to the exceptional hydration of the stratosphere by this phreatomagmatic eruption. An unusual aerosol fine mode (peak radius in 0.3-0.5  $\mu\text{m}$ ) is identified at 20 stations of the southern hemisphere until May 2023 (time of writing). Nevertheless, 1.4 years after eruption, HT-HH sulfate aerosols remain smaller than Pinatubo particles. Smaller aerosols backscatter more efficiently visible light and sediment more slowly than larger particles, implying stronger and longer-lasting negative radiative forcing.

**Plain Language Summary**

Explosive eruptions can inject large amounts of sulfate aerosols in the stratosphere, that may perturb atmospheric chemistry and Earth's climate. However, crucial information regarding the size of aerosols, a critical parameter in climate models, is generally missing. We address this gap for the eruption of Hunga Tonga-Hunga Haápai (HT-HH) in 2022, a record-breaking eruption in the satellite era. Based on an exhaustive analysis of satellite observations together with photometric ground observations from the worldwide open-access AERONET network, we document a rapid growth of HT-HH aerosols in the days following eruption. This early aerosol growth rate is faster than observed for 1991 Pinatubo, likely due to the exceptional humidification of the stratosphere caused by the water-rich HT-HH eruption. Furthermore, the year-long persistence of an unusually fine type of aerosols (i.e. with radius  $\sim 0.4 \mu\text{m}$ ) is identified at 20 stations of the southern hemisphere and used as a volcanic marker of the HT-HH plume. One year after eruption, and in spite of an initially rapid growth, HT-HH sulfate aerosols remain smaller than Pinatubo particles. Smaller particles better reflect sunlight and remain in suspension in the stratosphere for a longer time, fostering surface cooling.

**1 Introduction**

Since the 1991 eruption of Pinatubo (Philippines, 15°N, 120°E), long-lived stratospheric sulfate aerosols produced by high-magnitude explosive eruptions are known to modify atmospheric chemistry, dynamics and Earth's radiation balance (McCormick et al., 1995; Robock, 2000; Kremser et al., 2016; Marshall et al., 2022).

The eruption of Hunga Tonga-Hunga Haápai (HT-HH, 20.5°S, 175.4°W, Fig. 1) in January 2022 represents a record-breaking eruption in the satellite era, whose impact on climate remains to be assessed. Its phreatomagmatic nature fueled an exceptional explosive activity, with plume parcels reaching up to 57 km of altitude (Carr et al., 2022; Taha et al., 2022; Proud et al., 2022), leading to the largest aerosol perturbation of the stratosphere since the Pinatubo eruption (Sellitto et al., 2022; Legras et al., 2022). Considerable amounts of water vapour injected high into the atmosphere induced exceptional hydration of the stratosphere (Millan et al., 2022; Schoeberl et al., 2022; Vömel et al., 2022) and modifications in atmospheric circulation (Coy et al., 2022). However, the modest mass budget of  $\text{SO}_2$  emitted dur-

62 ing the paroxysmal phase of the eruption on 15 January 2022 (0.4-0.5 Tg, Carn et al. (2022),  
63 compared to  $\approx 20$  Tg during Pinatubo eruption, Bluth et al. (1992)), is in apparent contra-  
64 diction with the strong explosivity of the eruption. Apart from potential bias in the satel-  
65 lite retrieval of  $\text{SO}_2$  in presence of a large particle load in the plume, and acknowledging the  
66 probable amplification of explosivity due to magma-water interaction, this low  $\text{SO}_2$  budget  
67 raises the possibility of a fast conversion of  $\text{SO}_2$  into secondary sulfate aerosols.

68 The impact on climate of large eruptions can be evaluated with model simulations, but  
69 this approach is subject to uncertainty due to scarcity of direct observations of time-varying  
70 microphysical properties of stratospheric aerosols (Mann et al., 2015). Balloon-borne exper-  
71 iments are useful to provide direct constraints on the size distribution of stratospheric aerosols  
72 with altitude but, due to operational difficulty, cannot capture the detailed spatio-temporal  
73 evolution of aerosol microphysics (Deshler, 2008). Satellite occultation or limb-scattering mea-  
74 surements require prerequisite assumptions on particle size distribution or chemical compo-  
75 sition (Wrana et al., 2021; Taha et al., 2021; Bourassa et al., 2023).

76 Here, we analyze open-access data from the AERONET ground network of photome-  
77 ters that provide, at  $>600$  stations worldwide, information on the optical, microphysical and  
78 absorption properties of aerosols in the atmospheric column (B. Holben et al., 2001; Dubovik  
79 et al., 2002). Photometric observations have already provided information on the size distri-  
80 bution of volcanogenic stratospheric aerosols in the past decades. Originally, Asano et al. (1993)  
81 derived the radius of Pinatubo aerosols from spectral AOT measurements at one single sta-  
82 tion in Japan. Using volume size distributions retrieved at a few AERONET sites, B. Hol-  
83 ben et al. (1996) and T. F. Eck et al. (2010) highlighted an unusual “middle mode” (between  
84 the usual fine and coarse modes) associated with Pinatubo aerosols. Stothers (2001) evalu-  
85 ated the post-eruption effective radius ( $r_{eff}$ ) of fine aerosols from ground-based spectral ex-  
86 tinction measurements for the seven largest aerosol-producing volcanic eruptions in the twen-  
87 tieth century. N. T. O’Neill et al. (2012) followed the properties of stratospheric sulfate aerosols  
88 from the 2009 Sarychev eruption using measurements from Eureka AERONET station and  
89 polar sites of Ny-Alesund and Opal. More recently, Ridley et al. (2014) highlighted the in-  
90 fluence of moderate eruptions in the low stratosphere on the decadal trend in stratospheric  
91 aerosol optical depth (AOD).

92 Together with satellite observations (S5P/TROPOMI, MetOp-B and MetOp-C/IASI,  
93 HIMAWARI-8/AHI, CALIPSO/CALIOP), we analyse aerosol properties derived from pho-  
94 tometric data collected at 20 stations of the southern hemisphere to characterize and track  
95 the persistence of volcanic aerosols associated with HT-HH eruption.

## 96 2 Observations and methodology

97 A set of observations of volcanic sulfur dioxide ( $\text{SO}_2$ ) gas and particles, from passive sen-  
98 sors onboard low earth orbit and geostationary satellites as well as active spaceborne LIDAR,  
99 is analysed. It includes  $\text{SO}_2$  vertical column amounts (15 km product) from high spectral and  
100 spatial resolution ultraviolet observations from Sentinel-5P/TROPOspheric Monitoring In-  
101 strument (TROPOMI) with a pixel size of 7 km x 3.5 km at nadir (Theys et al., 2017, 2019).  
102  $\text{SO}_2$  height products, derived from observations of the Infrared Atmospheric Sounding Inter-  
103 ferometer (IASI) onboard MetOp-B and MetOp-C polar orbiting satellites (footprint of 12  
104 km at nadir) (Clarisse et al., 2014), also allow us to track four times a day the HT-HH plume  
105 and over a longer period of time than using  $\text{SO}_2$  column amounts. Near-source particle prop-  
106 erties are explored using SEVIRI-like ash RGB compositions derived from geostationary L1B

107 brightness temperatures of HIMAWARI-8/AHI (Advanced Himawari Imager) at 8.6, 10.4 and  
 108 12.4  $\mu\text{m}$  channels available every 20 minutes (EUMETSAT, 2023; Japan Meteorological Agency,  
 109 2023) as well as observations from the spaceborne CALIPSO/Cloud-Aerosol Lidar with Or-  
 110 thogonal Polarization (CALIOP) including total attenuated backscatter at 532 nm and de-  
 111 polarization ratio (Winker et al., 2009).

112 Regarding ground-based observations, we analyze cloud-screened Level 1.5 observations  
 113 (version 3, Giles et al. (2019)) from the worldwide AERONET network of sun/sky radiome-  
 114 ters (B. N. Holben et al., 1998; B. Holben et al., 2001), with a focus on a selected subset of  
 115 20 stations in the southern hemisphere. Quasi-continuous direct sun measurements, with a  
 116 sampling interval of 5 to 15 minutes (under cloudless conditions), provide AOD and Angstrom  
 117 exponent values (B. N. Holben et al., 1998; B. Holben et al., 2001) as well as the partition  
 118 of  $\text{AOD}_{500\text{nm}}$  between fine and coarse mode particles using the SDA algorithm (N. O’Neill  
 119 et al., 2003). Measurements are collected both in daylight and at night using lunar photom-  
 120 etry (Barreto et al., 2016).

121 Using the same ground-based instruments, sky radiance measurements are also retrieved  
 122 in the almucantar geometry (e.g. fixed elevation angle equal to solar elevation, and full  $360^\circ$   
 123 azimuthal sweep) at various wavelengths (440, 670, 870 and 1020 nm). These multi-angular  
 124 and multi-spectral observations are modeled with a radiative transfer model combined with  
 125 a microphysical description of light scattering by particles, and inverted using a procedure  
 126 incorporating smoothness constraints on spectral and size distributions as well as a robust  
 127 statistical noise model (Dubovik & King, 2000; Dubovik et al., 2002). The algorithm provides  
 128 a detailed evaluation of the volume size distribution (VSD), absorption (single scattering albedo,  
 129 SSA) and complex refractive index of aerosols (Dubovik & King, 2000; Dubovik et al., 2000,  
 130 2002, 2006; B. N. Holben et al., 2006; Torres et al., 2014). In Version 3 of the algorithm, aerosols  
 131 are assumed to be partitioned into two classes including spherical and non-spherical compo-  
 132 nents (Dubovik et al., 2006). The spherical component is modeled by polydispersed homo-  
 133 geneous spheres with the same complex refractive index. The non-spherical component is a  
 134 mixture of polydisperse, randomly-oriented homogeneous spheroids. Importantly, accuracy  
 135 of VSD retrieval is maintained for  $\text{AOD}_{440\text{nm}}$  down to 0.02, compared to  $\text{AOD}_{440\text{nm}} > 0.4$  for  
 136 SSA (Sinyuk et al., 2020). Nevertheless, edges of the aerosol VSD (radius  $< 0.1 \mu\text{m}$  and  $>$   
 137  $7 \mu\text{m}$ ) are less constrained because of the low sensitivity of the aerosol scattering at the wave-  
 138 lengths that are measured for these sizes of aerosols. However, the size of HT-HH aerosols  
 139 belongs to the range of aerosol size retrieved with the highest accuracy (retrieval error  $< 10\%$   
 140 for maxima of the VSD, Dubovik et al. (2002)). In summary, even if less frequent than di-  
 141 rect measurements due to restrictive quality criteria, almucantar measurements give access  
 142 to the complete volume size distribution of aerosols with minimal constraints. Throughout  
 143 the paper, selected data fulfill quality criteria (sky residual  $< 10\%$ ,  $\text{SZA} < 70^\circ$ ). A low sky resid-  
 144 ual ensures that aerosol properties are homogeneous at the scale of the Almucantar field of  
 145 view.

146 In common atmospheric conditions, two local maxima of the VSD are found, classically  
 147 referred to as the “fine mode” and the “coarse mode”. The standard AERONET processing  
 148 provides the effective radius for each mode, noted  $r_{eff}$ , which represents an integral quan-  
 149 tity over each sub-distribution, eg. the ratio of the skewness to the variance of the particle  
 150 number distribution (T. Eck et al., 1999). However, the effective radius brings a blurred vi-  
 151 sion in the case of overlapping size distributions within a specific mode (T. F. Eck et al., 2010),  
 152 which may arise in the event of a volcanic eruption.

153 Alternatively, in order to identify the volcanic modes associated with HT-HH aerosols,  
 154 we search for the local maxima of the aerosol VSDs after applying a spline interpolation. This

155 approach is intended to better achieve the detection and separation of sub-populations of aerosols  
 156 that may coexist in the atmospheric column, regardless of the actual shape of the underly-  
 157 ing size distribution. The method uses as input the almucantar-derived VSD provided by AERONET,  
 158 noted  $v_j$ , sampled in 22 bins centered on radii  $r_j$  (where  $j$  is the index of the bin) with a reg-  
 159 ular logarithmic progression between  $0.05 \mu\text{m}$  and  $15.0 \mu\text{m}$ . A cubic-spline fitting of  $v_j$  is per-  
 160 formed, yielding an interpolated spline object  $\mathbf{f}$  (ie. a piecewise cubic polynomial function),  
 161 such that  $\mathbf{f}(r_j) = v_j, \forall j$ . Note that  $\mathbf{f}$  can be evaluated at any  $r$  in each  $[r_j, r_{j+1}]$  interval,  
 162 potentially overshooting slightly above  $v_j$  or  $v_{j+1}$ . Nevertheless, because the  $v_j$  are regularly  
 163 spaced and already “smooth”, the overshoot effect remains contained.

164 After interpolation, all local maxima of  $\mathbf{f}$  on the  $[0.05-15.0]\mu\text{m}$  interval are calculated:

$$r_{peak} = \underset{r \in S}{\text{arg localmax}} \mathbf{f}(r), \text{ with } S = [0.05, 15.0] \mu\text{m} \quad (1)$$

165 Local maxima occurring at interval endpoints ( $0.05 \mu\text{m}$  and  $15.0 \mu\text{m}$ ) are discarded a pos-  
 166 teriori to avoid side effects. The number of remaining local maxima depends on the shape of  
 167  $v_j$ , and varies between one, when a single peak dominates the distribution, and, exception-  
 168 ally, up to five. However, in most profiles, two local maxima are found, representing the fine  
 169 mode and the coarse mode. After the HT-HH eruption, as discussed later, a third local max-  
 170 imum becomes visible on a number of stations.

171 When several peaks are found, they are sorted by decreasing order of their respective  
 172 amplitude in the VSD. In other words, for each almucantar-derived VSD, the method extracts  
 173 a list of local maxima of the interpolated VSD, indexed by integer  $i$ , each with a radius  $r_{peak,i}$   
 174 and an amplitude  $A_{peak,i}$ . Hence,  $r_{peak,1}$  is the radius of largest peak in the VSD with am-  
 175 plitude  $A_{peak,1}$ , then  $r_{peak,2}$  is the second-largest peak with amplitude  $A_{peak,2} < A_{peak,1}$ ,  
 176 and so forth. The value of  $A_{peak,i}$  is the “height” of the VSD for the mode corresponding to  
 177 the peak with index  $i$ , and can be interpreted as a proxy of the particle abundance, for this  
 178 particular peak, in the atmospheric column above the station. VSDs with more than three  
 179 local maxima are found in situations with low particle abundance, close to the measurement  
 180 noise, so that peaks with indexes  $i \geq 4$  can be ignored. The width of the bins, which varies  
 181 logarithmically with the radius, can be taken as a conservative estimate of the uncertainty  
 182 of the retrieved  $r_{peak}$ . To give numerical values relevant to the HT-HH volcanic range, bin  
 183 width increases from  $\sim 0.07 \mu\text{m}$  at  $r_{peak} = 0.25\mu\text{m}$ , to  $\sim 0.16 \mu\text{m}$  at  $r_{peak} = 0.57\mu\text{m}$ .

185 The joint interpretation of satellite and ground-based remote sensing observations of  
 186 the HT-HH plume, as well as multi-station data analysis, are performed using the VOLCPLUME  
 187 interactive web portal (Boichu & Mathurin, 2022), that was used in crisis time to deliver in-  
 188 formation on HT-HH aerosols (Vernier et al., 2022; Lac et al., 2022).

### 189 3 Results

#### 190 3.1 Evolution of sulfate aerosols size during the first circumnavigation of the 191 globe

##### 192 3.1.1 Rapid growth (15–22 January 2022)

193 Near-source satellite and ground-based observations in Fig. 1 illustrate the spatio-temporal  
 194 evolution of  $\text{SO}_2$  and particles emitted by the explosive HT-HH eruption on 15 January 2022  
 195 until their overpass over Australian land surfaces that are instrumented with ground-based

196 sun/sky radiometers of the AERONET network. Joint comparison of satellite and ground-  
 197 based data is essential to pinpoint the precise time of overpass by the plume, and associate  
 198 unambiguously any anomaly in ground measurements to a volcanic origin.

199 The explosive eruption of HT-HH starts on 15 January 2022 around 04:00 UTC (Fig.  
 200 1a1), according to the first plume detection illustrated by Himawari-8/AHI observations at  
 201 04:20 UTC (Fig. S1 and Movie S1). Coarse particles near the volcanic source are highlighted  
 202 by dark colors (brownish/blue/black) in ash RGB compositions (Fig. 1a1 and a2) indicat-  
 203 ing presence of ice crystals, sea salts or coarse ash particles (EUMETRAIN, 2023). A rapid  
 204 change in plume characteristics, shifting from dark (Fig. 1a1 and 1a2) to light green (Fig. 1a3  
 205 and 1a4) colors, indicates a predominant abundance of SO<sub>2</sub> and sulfate aerosols in the HT-  
 206 HH plume (e.g. from 16 Jan 2022 00:00 UTC, Fig. 1a3), supporting near-source modifica-  
 207 tion of the physico-chemical properties of the HT-HH plume. This change may explain the  
 208 disappearance of coarse particles, possibly resulting from sedimentation/wet aggregation pro-  
 209 cesses (Textor et al., 2006; Folch et al., 2010) and/or dilution of the dispersed plume induc-  
 210 ing a decaying signal from small ash particles (<few microns) below the detection threshold  
 211 of geostationary infrared observations (Prata, 1989), as also discussed by Legras et al. (2022).

212 TROPOMI observations on 17 January (from 00:00 to 05:00 UTC) confirm quantita-  
 213 tively the detection of the SO<sub>2</sub>-rich HT-HH plume reaching Australia (Fig. 1b), so far qual-  
 214 itatively imaged with Himawari-8/AHI (Fig. 1a4). Approximately ten hours before this TROPOMI  
 215 acquisition (16 January 15:41 UTC), CALIPSO/CALIOP observations detect aerosols in the  
 216 HT-HH plume passing over the Coral Sea (Fig. 1d). CALIOP observations indicate that the  
 217 plume is mainly composed of poorly-depolarizing (e.g. almost spherical, depolarization ra-  
 218 tio <3%, Fig. S2) aerosols in the stratosphere, hence suggesting a young plume already rich  
 219 in sulfate aerosols. The vertical distribution of HT-HH aerosols is complex with distinct parcels  
 220 at, at least, two distinct altitudes (Fig. 1d): one parcel at 26-29 km asl (with a weaker sig-  
 221 nal indicating presence of aerosols around 23-24 km), another parcel, further south, at 30-  
 222 32 km asl. Nevertheless, we cannot exclude the presence of aerosols at a higher altitude at  
 223 that time, with potentially different properties. Indeed, CALIOP detected higher altitude aerosols  
 224 (between 35-40 km) earlier on 15 January with strongly depolarizing properties supporting  
 225 the presence of ash and/or ice (Khaykin et al., 2022). Taha et al. (2022) also report the pres-  
 226 ence of such high altitude aerosols (>36.5 km) over Australia on 17 January from OMPS-LP  
 227 observations. The persistence of volcanic aerosols at altitudes >36 km is observed with OMPS-  
 228 LP up to 27 January 2022 with a decaying aerosol extinction ratio anomaly (Taha et al., 2022).  
 229 However, OMPS-LP data do not provide information on the depolarizing properties of these  
 230 transient high-altitude particles.

231 Eastern Australia hosts the first AERONET photometric station (Lucinda) flown over  
 232 by the plume (Fig. 1c). By analysing the aerosol volume size distributions coinciding with  
 233 the SO<sub>2</sub> plume overpass, along with the AOD partitioning between fine and coarse mode, de-  
 234 tailed information on the microphysical and radiative properties of HT-HH aerosols can be  
 235 deduced (Fig. 2). An excess AOD anomaly peaking at about 2 (at 440 nm) is recorded on  
 236 late 16 January 2022 at 21:36 UTC, largely above background values (Fig. 1c). These high  
 237 AOD values are mainly caused by fine particles (radius <0.5 μm) (Fig. 2b2), while the coarse  
 238 AOD only slightly departs from background (Fig. 2b3, see also Section 4.2). Inversions of al-  
 239 mucantar observations, collected on 16 January 2022 at 22:10 and 22:36 UTC, confirm the  
 240 abundance of fine particles, with volume concentrations greater by a factor of ≈ 30 relatively  
 241 to background conditions (Fig. 2c). However, their size ( $r_{eff}$  ranging in 0.22-0.23 μm, Fig.  
 242 2c) is significantly larger than background aerosols observed before the plume overpass (0.12  
 243 μm), exceeding the historical monthly-mean ( $\pm 1\sigma$ ) range (0.11–0.17 μm, blue shaded area

in Fig. S3.1). Furthermore, these fine aerosols are poorly-absorbing, with a  $SSA_{440nm}$  ranging in 0.97–0.98, much higher than recorded early morning 12 hours before the HT-HH plume overpass ( $SSA_{440nm}$  of 0.85), and in the upper bound of historical monthly-mean SSA values (0.78–0.98, red shaded area in Fig. S3.1). Given  $AOD_{440nm} \gg 0.5$ , the complex refractive index of these aerosols can be retrieved, with a real part shown to vary between 1.33 at 440 nm and 1.35 at 1020 nm and a constant imaginary part ranging in 0.003–0.004. Therefore, the abundant presence of poorly-absorbing fine aerosols indicates high concentrations of sulfate aerosols within the HT-HH young plume (about 42 hour-old plume).

On 19 January, a broader peak in  $AOD_{500nm}$ , reaching  $\approx 1$ , lasting about 12 hours, is recorded in western Australia (Learmonth), 7000 km from source (Fig. 2b). The plume then reaches the stations of Maido OPAR and Saint-Denis on La Réunion island on 21 January (Fig. 2a2), 13000 km from source, with an  $AOD_{500nm}$  up to 0.6 for two days (Fig. 2b). The timing of the AOD peak detection at stations Lucinda, Learmonth and Maido is consistent with the translation of the volcanic plume visible in  $SO_2$  satellite imagery (Fig. S4). Furthermore, the broadening of the AOD peak toward the west, as well as the decrease of the peak amplitude toward the west, are consistent with a progressive elongation and dispersion of the plume during transport over the Indian Ocean.

Whichever the station, these high total AOD values are mainly caused by fine particles (Fig. 2b). Again, a few almucantar observations provide detailed volume size distribution and absorption properties of aerosols measured over each station (Fig. 2c). In western Australia (Learmonth), fine mode  $r_{eff}$  of  $0.33 \mu m$  is recorded on 19 January 2022, much larger than monthly-mean background values ( $0.14$ – $0.20 \mu m$ , Fig. S3.2), with  $SSA_{440nm}$  of 0.98 far exceeding the monthly background ( $0.82$ – $0.93$ , Fig. S3.2). A few days later on 22 January 2022, fine mode aerosols with  $r_{eff}$  of  $0.39 \mu m$  are observed in La Réunion (Maido OPAR), much larger than monthly background values ( $0.12$ – $0.23 \mu m$ ), with  $SSA_{440nm}$  of 0.98 (Fig. S3.3). These observations indicate the growth of an unusual fine mode of poorly-absorbing particles, likely sulfates, almost doubling in size over their 7-days transport from eastern Australia (Lucinda) to La Réunion.

### 3.1.2 Stabilization of particle size (22–31 January 2022)

One week following the eruption, zonal progression of the HT-HH plume can be tracked by the successive occurrence of excess AOD anomalies, sweeping across the global ground-based AERONET network from east to west. Fig. 3 shows the spatio-temporal evolution of detections of excess fine AOD anomalies for a subset of nine AERONET stations situated within a latitudinal belt roughly centered on  $20^\circ S$ , which are all overpassed during the first circumnavigation of the globe by the  $SO_2$ -rich plume. To select these stations, we first systematically examined the pre- and post-overpass records at all stations in the  $10^\circ$ – $30^\circ S$  latitudinal band, and searched for an anomaly in properties of the fine mode, ie. affecting simultaneously both the AOD and the effective radius. Successive  $SO_2$  maps produced by satellite imagery allowed us to correlate these anomalies with the presence of the volcanic plume. However,  $SO_2$  conversion, in addition to dispersion and to dry/wet deposition, leads to decaying  $SO_2$  concentrations in satellite products (Fig. S4). Hence, in order to facilitate the ground-to-satellite comparison, instead of TROPOMI  $SO_2$ , we used  $SO_2$  detections derived from bi-daily IASI  $SO_2$  height products (Clarisse et al., 2014). For the aged plume (ie. 1 week – 2 weeks after eruption), we found that IASI  $SO_2$  height products achieve a lower detection threshold than TROPOMI  $SO_2$  column amounts, and therefore bring a greater confidence for tracking the time of overpass of the dispersed HT-HH plume above ground stations (Fig. 3a).



290 In Africa, the first excess fine AOD anomalies are detected by AERONET stations in  
 291 Mozambique (Niassa) on 21 January, then in Namibia and South Africa on 24–25 January  
 292 (Windpoort, Metsi, Gobabeb) (Fig. 3b). Anomalies are then detected first on 26 January along  
 293 the Atlantic coast of Brazil (SP-EACH), and finally on the Pacific side of the South Amer-  
 294 ican continent (PSDA-Chile) (Fig. 3b). To the extent made possible by the uneven tempo-  
 295 ral resolution involved in the correlation between SO<sub>2</sub> satellite images (revisit time of 12 hours  
 296 for IASI) and direct sun measurements by ground stations, we find that the timing of detec-  
 297 tion of fine AOD anomalies from the ground coincides precisely with the overpass by the strato-  
 298 spheric HT-HH plume (Fig. 3). For a given longitude, the lag between stations located at dif-  
 299 ferent latitudes is well explained by the complex shape of the plume, as illustrated in Fig. 3a  
 300 and Fig. 4 for Metsi station (South Africa).

301 The temporal coincidence between (a) detection of an anomaly in fine AOD from ground-  
 302 based AERONET measurements, and (b) overpass by the SO<sub>2</sub> plume (as deduced from satel-  
 303 lite imagery) indicates that ground-based AERONET measurements can be exploited to pro-  
 304 vide quantitative information about the characteristics of volcanic aerosols in the stratosphere,  
 305 in particular their size thanks to almucentar inversions. For a number of stations in Africa  
 306 and South America, a jump in the fine mode effective radius  $r_{eff}$  is distinctly visible in the  
 307 time-series (Fig. 3c), coinciding with a notable excess in fine mode AOD (Fig. 3b). The anomaly  
 308 is not visible at all stations, due to variability in the background records (pre-overpass) and/or  
 309 gaps in the records (lack of almucentar observations at the time of overpass by the plume).  
 310 At stations in Africa (Niassa, Metsi, Windpoort and Gobabeb) and in South America (SP-  
 311 Each, PSDA Chile), we observe fine mode  $r_{eff}$  ranging in 0.24-0.4  $\mu\text{m}$  during the plume over-  
 312 pass (Fig. 3c). We found that a threshold of  $r_{eff} > 0.22 \mu\text{m}$  was sufficient to detect the time  
 313 of appearance of the HT-HH overpass on the subset of nine stations (Fig. 3c). However, the  
 314 fine mode effective radius cannot be considered as a reliable indicator of the size of volcanic  
 315 particles when different populations of fine particles coexist within the atmospheric column.

316 In Fig. 4, we illustrate such a case with the African station of Metsi. Before the over-  
 317 pass of the station by the HT-HH plume (illustrated by IASI SO<sub>2</sub> detections in Fig. 4b), aerosol  
 318 VSDs on 24 January (green-blue lines in Fig. 4a) indicate the presence of very fine aerosols  
 319 with  $r_{eff} = 0.15\text{--}0.16 \mu\text{m}$  (Fig. 4c). One day later (25 January), as the HT-HH plume flies  
 320 over the station (Fig. 4b), the particle size distribution shows the presence of a new aerosol  
 321 mode of volcanic origin in the fine range, in addition to the very fine mode characteristic of  
 322 “background” aerosols (orange line in Fig. 4a). This volcanic mode is, at this time, more abun-  
 323 dant than the background mode. However, only a slight increase of the fine mode effective  
 324 radius is observed, reaching only 0.24  $\mu\text{m}$  (Fig. 4c).

325 Therefore, instead of relying on  $r_{eff}$ , we seek for anomalies in the location of the peaks  
 326 in the VSD, which is a more reliable indicator in the presence of two (or more) sub-populations  
 327 with overlapping distributions. In such a situation, contrary to the fine mode  $r_{eff}$ , the aerosol  
 328 parameter  $r_{peak}$  (defined in Section 2) allows for separating the two populations, by provid-  
 329 ing a more accurate estimate of the volcanic aerosol radius  $r_{peak-volc}$  and possibly also the  
 330 background aerosol size  $r_{peak-background}$ . The  $r_{peak-volc}$  parameter is expected to be very sim-  
 331 ilar to the effective radius  $r_{eff-volc}$  associated purely with the population of volcanic aerosols  
 332 that can directly be measured with other methods such as in situ measurements. This ap-  
 333 proach is applied systematically for the identification of HT-HH sulfate aerosols over Africa  
 334 and South America. The strategy involves finding the radius  $r_{peak}$  of the aerosols giving the  
 335 largest contribution to the VSD fulfilling quality criteria (AOD > 0.1, sky residual < 10%).

At Metsi, this method highlights the coexistence of two distinct classes of fine aerosols on 25 January: (1) a very fine mode with  $r_{peak-background} = 0.12 \mu\text{m}$ , a value similar to the effective radius measured in background conditions, and (2) a larger fine mode of volcanic origin with  $r_{peak-volc} = 0.45 \mu\text{m}$  (Fig. 4c). The next day (26 January), the radius of the volcanic particles remains similar, with  $r_{peak-volc}$  ranging in 0.39-0.42  $\mu\text{m}$  (Fig. 4c).

Globally, after a rapid growth of sulfate aerosols almost doubling in size from eastern Australia to La Réunion, no further growth of HT-HH aerosols is observed over Africa or South America (Fig. 5). From 24 to late January 2022, stations in Africa, and then in South America, indicate aerosol  $r_{peak-volc}$  slightly smaller (ranging in [0.36–0.47]  $\mu\text{m}$ ) than at La Réunion (0.46  $\mu\text{m}$ ). Hence, although HT-HH plume gets more dispersed and diluted with time, in coherence with broadly decaying  $\text{SO}_2$  concentrations and decreasing fine AOD (Fig. 3b), the size of the volcanic fine aerosols remains relatively stable (Fig. 5). Slight differences in aerosol size among different stations probably results from complexity in plume spatial distribution, in terms of  $\text{SO}_2$ /aerosol/water concentration and altitude, possibly reflecting some second-order heterogeneity in growth rate and composition.

### 3.2 Year-long persistence of HT-HH sulfate aerosols in southern hemisphere

From February 2022 to May 2023 (time of writing), we seek for the presence of an anomaly, presumably of volcanic origin, by analyzing the aerosol VSD derived from AERONET almu-cantar measurements. Fig. 6 displays the temporal evolution of aerosol VSD at La Réunion/Maido OPAR station, a high-altitude station (2160 m a.s.l.) in the Indian Ocean with a relatively pristine atmosphere (Koren et al., 2014). The volcanic signature is manifested by a change in the shape of the VSDs at the time of the eruption, with the emergence of a new mode, hereafter called “volcanic fine mode” or “volcanic mode”, situated in the interval between the traditionally observed “fine” and “coarse” modes (Fig. 6a). This rare feature in the AERONET database is reminiscent of the “middle mode” previously documented for Pinatubo aerosols (B. Holben et al., 1996; T. F. Eck et al., 2010) and for desert dusts in Niger and Bodele Depression of central Chad (Tanré et al., 2001; T. F. Eck et al., 2010).

The volcanic mode produces an additional local maximum  $r_{peak}$  in the VSD around 0.4  $\mu\text{m}$ , which can be tracked with time, as shown in Fig. 6b for station La Réunion/Maido OPAR. There, the  $r_{peak}$  anomaly is first visible on 22 January during the first HT-HH plume overpass (★ in Fig. 6, as discussed in Section 3.1.1). Then, after a temporary lull as the plume makes its first circumnavigation around the globe (◆ in Fig. 6), the volcanic anomaly becomes visible again from 9 February 2022 (♣ in Fig. 6). After February 2022, the volcanic aerosol fine mode anomaly remains continuously visible in the VSDs of La Réunion/Maido OPAR up to May 2023 (time of writing). The anomaly is also identified by comparing the density frequency histograms of aerosol radius in the fine range before and after the eruption (right hand side of Fig. 6b). The year-long persistence of this volcanic mode, here documented at the AERONET station of La Réunion/Maido OPAR, is consistent with LIDAR ground-based observations performed at the same observatory, which detect HT-HH aerosols in November 2022 (Baron et al. (2023) and pers. comm. from V. Dufлот).

More broadly, manual search in the AERONET dataset reveals that the volcanic mode is detected at a total of (at least) 20 stations (including Maido OPAR) of the southern hemisphere (Fig. 7). These stations are located at latitudes ranging from 12°S (Mozambique/Niassa) to 46°S (Argentina/CEILAP Comodoro), in different continents and regions (Africa, South America, Australia, western Pacific region), and contrasted atmospheric environments. Us-

381 ing the same representations as in Fig. 6, VSDs (covering both fine and coarse modes) are  
 382 shown at all 20 stations in Fig. S6 and the time-series of  $r_{peak}$  in Fig. S7 to S9.

383 This volcanic mode, with  $r_{peak}$  ranging in  $[0.28-0.50]$   $\mu\text{m}$ , persists after eruption for a  
 384 minimum of 16 months (at the time of writing). It is distinct from background fine mode aerosols  
 385 visible in the months prior to eruption, which have generally a smaller size ( $<0.30$   $\mu\text{m}$ ). How-  
 386 ever, in periods of enhanced background aerosol load, the volcanic signal may be temporar-  
 387 ily lost. For instance, at Maido OPAR, as well as other stations in the Southern part of Africa  
 388 (Fig. S8), the background aerosol load increases every year from September to November, tem-  
 389 porarily obscuring the volcanic mode ( $\spadesuit$  in Fig. 6). This period of enhanced AOD likely re-  
 390 sults from long-range transport of aerosols from biomass burning fires in southern Africa (and  
 391 possibly Madagascar), which have been shown to impact ozone and carbon monoxide con-  
 392 centrations at La Réunion at that time of the year (Randriambelo et al., 2000; Clain et al.,  
 393 2009; Foucart et al., 2018). On the other hand, detection is achieved even at stations affected  
 394 by high levels of desert dust and/or sea salt (eg., Australia/Learmonth, Namibia/Gobabeb,  
 395 Fig. 7 and S6), suggesting that the HT-HH volcanic signal is less perturbed by the presence  
 396 of coarser particles.

397 For all four stations with enough data situated to the south of  $\sim 33^\circ\text{S}$  (AU NSW Lid-  
 398 combe, Univ of Auckland, Trelew, CEILAP-Comodoro), the volcanic mode becomes visible  
 399 in the time series of  $r_{peak}$  only after a time lag of several months, e.g. 3 months after erup-  
 400 tion over Australia/AU NSW Lidcombe station ( $34^\circ\text{S}$ ) and 4 months over Argentina/Trelew  
 401 station ( $43^\circ\text{S}$ ) (Fig. 7). At these stations, the time lag is also visible in the amplitude of the  
 402 maximum of the VSD in the volcanic fine range ( $0.22-0.90$   $\mu\text{m}$ ), which also increases from  
 403 April–June 2022 at these southerly stations. This coincidence indicates an increase of the aerosol  
 404 load in the atmospheric column prompted by the progressive influence of the HT-HH aerosols  
 405 (Fig. S10). This latency for high-latitude stations suggests that it takes several months for  
 406 the plume to reach high (southern) latitudes.

407 In order to assess the temporal variations of the HT-HH aerosol properties at the scale  
 408 of the southern hemisphere, we stack observations from all 20 stations of Fig. 7. We first stack  
 409 the amplitudes  $A_{peak}$  of the peaks falling within the volcanic mode size range, ie.  $[0.22-0.90$   
 410  $\mu\text{m}]$  (Fig. 8a). This “amplitude stack” can be interpreted as a proxy of the evolution of the  
 411 column-integrated abundance of volcanic particles across the southern hemisphere. Only the  
 412 radii falling with the interval  $[0.22-0.90$   $\mu\text{m}]$  are considered in the stack, in order to avoid in-  
 413 terference with the non-volcanic fine or coarse background aerosols. We also stack the aerosol  
 414 radii  $r_{peak,i}$  at these 20 stations (Fig. 8b). These stacks show that, from the eruption until  
 415 May 2023 (time of writing), HT-HH aerosol  $r_{peak}$  values range in  $0.35-0.5$   $\mu\text{m}$  (Fig. 8b). Un-  
 416 til June 2022, an overall decrease in particle size is observed (Fig. 8b), coinciding with an or-  
 417 der of magnitude decrease in  $A_{peak}$  (Fig. 8a). During the same period of time, the scatter  
 418 between values of  $r_{peak}$  at different stations tends to decrease, giving way to a narrow band  
 419 in the stack of  $r_{peak}$  (dashed lines in Fig. 8b). Concomitantly, after June 2022, the ampli-  
 420 tude  $A_{peak}$  in the volcanic range stabilizes to a nearly constant value of  $0.005$   $\mu\text{m}^3 \cdot \mu\text{m}^{-2}$  for  
 421 all stations (Fig. 8a). This behavior likely reflects the progressive homogeneization of the HT-  
 422 HH aerosol layer from January to June 2022, as VSDs at stations affected by the volcanic fin-  
 423 gerprint tend to converge to a common shape and amplitude, hence yielding a geographically-  
 424 uniform peak radius and peak amplitude. Given the spatial distribution of the stations, this  
 425 hypothesis of an homogeneization of the HT-HH aerosol layer most likely extends to the scale  
 426 of the southern hemisphere, at least down to  $45^\circ\text{S}$ . Accordingly, this strategy is warranted  
 427 by the consistency of anomalies among selected stations, which allows for overcoming the ex-  
 428 istence of data gaps in individual time-series.

After June 2022, slow temporal variations of the HT-HH aerosol size are observed (Fig. 8b), with a minimum radius of  $0.35 \mu\text{m}$  reached in July 2022, followed by a progressive increase up to  $0.50 \mu\text{m}$  in late January 2023, and finally a slight decrease up to May 2023 (time of writing). The change of  $r_{peak}$  in late January 2023 appears to coincide with a drop of the amplitude  $A_{peak}$ , whose origin is uncertain due to lack of hindsight. Understanding the origin of these second order fluctuations would require further investigation.

## 4 Discussion

### 4.1 Estimated ranges of HT-HH aerosol size

In the 1 year-long timeseries of HT-HH sulfate aerosol size derived from AERONET photometric observations at 20 stations in the southern hemisphere, we report the detection of a volcanic fine mode with sub-micronic size (Fig. 8). The smallest particles, with a peak radius in  $0.22\text{--}0.26 \mu\text{m}$ , are observed in Eastern Australia,  $\sim 1$  day after eruption (Fig. 2, 3 and 5), whereas particle size in subsequent measurements stabilizes to  $\sim 0.4\text{--}0.5 \mu\text{m}$  within  $\sim 1$  week after the eruption (Fig. 5).

Comparison with other studies can be attempted on the basis of these size estimations, but requires careful consideration of the time and space frame of the comparison, as well as an understanding of uncertainties underlying each analysis. AERONET measurements provide estimates of size distribution integrated over the vertical column, hence do not allow for constraining the vertical distribution of aerosol properties. Furthermore, AERONET measurements are, by nature, punctual in space and intermittent in time. Hence, spatial heterogeneity of the HT-HH plume in the first weeks following the eruption precludes a direct translation of ground-based observations into averaged properties of the plume, which can only be achieved once the plume has homogenized. Based on the temporal evolution of HT-HH aerosol radius (estimated from  $r_{peak}$ ), we estimate that this transient phase lasted for  $\sim 4$  months after the eruption (Section 3.2). Hence, until June 2022, heterogeneity of the aerosol layer may be easily invoked to explain, at least partly, any discrepancy between independent estimations of HT-HH aerosol properties. Nevertheless, the early stability of the aerosol radius, visible as early as  $\sim 1$  week after the eruption, elicits the comparison with previous studies that focused specifically on HT-HH aerosol size.

Based on AERONET observations, we measure an aerosol peak radius of  $0.46 \mu\text{m}$  ( $r_{eff}$  of  $0.39 \mu\text{m}$ ) at La Réunion/Maido OPAR station on 22 January 2022 (Fig. 2c). This result is in broad agreement with the sub-micronic size of HT-HH aerosols derived from balloon-borne LOAC in situ measurements, collected a few days later on 23 and 26 January 2022 at La Réunion (Kloss et al., 2022). Nevertheless, we also find at La Réunion/Maido OPAR an unusual aerosol coarse mode that is characterized by  $r_{eff}$  of  $4.6 \mu\text{m}$  on 22 January (Fig. S3.3). This is in line with a conspicuous spike in the coarse AOD at the neighboring AERONET station of Réunion St-Denis on 22 January 2022, around 02:00 UTC (Fig. 2b3). The absence of supra-micronic particles in Kloss et al. (2022) is only representative of measurements at their altitude of sampling (19–22 km altitude) and does not preclude the simultaneous presence of possibly larger particles traveling at higher or lower altitude. The coarse particles, with  $r_{eff}$  of  $4.6 \mu\text{m}$  at La Réunion, are not found in later measurements, possibly indicating the presence of a transient parcel, consistent with the relatively heterogeneous plume observed in the first days following the eruption. A more in-depth discussion of this scenario is provided in Section 4.2.

473 Another approach for estimating HT-HH aerosol size consists in attributing the decrease  
 474 of aerosol height with time to gravitational settling. Time-series of aerosol height are derived  
 475 from satellite measurements, such as CALIOP (Legras et al., 2022) and OMPS-LP (Schoeberl  
 476 et al., 2022; Khaykin et al., 2022). The height of the HT-HH stratospheric aerosol layer is shown  
 477 to slowly descend from  $\sim 24$ – $26$  km in February 2022 to  $\sim 21$ – $24$  km in July 2022. This de-  
 478 scent rate is then used to derive aerosol size estimations integrated over several months, based  
 479 on a number of assumptions. First, when aerosol and water plumes overlap, the air vertical  
 480 motion is determined by evaluating the ascent rate of the water plume, usually from MLS ob-  
 481 servations. When aerosol and water plumes do not overlap, Legras et al. (2022) use diabatic  
 482 and adiabatic ERA5 vertical velocities instead. Secondly, they subtract the air motion to the  
 483 aerosol descent rate so as to estimate the net aerosol sedimentation velocity. Thirdly, a sim-  
 484 plified model for particle fall speed is used to evaluate aerosol size from settling rate using  
 485 Stokes formula. Using this approach, preliminary analyses have estimated aerosol radii greater  
 486 than  $1 \mu\text{m}$ , which are hard to reconcile with our results: Schoeberl et al. (2022) report a ra-  
 487 dius of  $1.2 \mu\text{m}$  in March–June 2022, whereas Legras et al. (2022) estimate a decrease from  
 488  $2 \mu\text{m}$  in February 2022 to  $0.5 \mu\text{m}$  in late July 2022. In contrast, a more recent study by Khaykin  
 489 et al. (2022) yields a smaller aerosol radius of  $0.35$ – $0.54 \mu\text{m}$  in April–May 2022, which is fully  
 490 consistent with our findings.

491 Lastly, evaluation of monthly-mean aerosol size is provided by fitting a lognormal size  
 492 distribution to SAGE-III/ISS satellite extinction spectra (Khaykin et al., 2022). The infor-  
 493 mation content of such spaceborne observations is insufficient to retrieve simultaneously aerosol  
 494 size and composition as they both affect spectra inversion. For this reason, the distribution  
 495 with altitude of the monthly-mean aerosol effective radius, averaged for a range of latitude  
 496 in  $10$ – $30^\circ\text{S}$ , is provided assuming different aerosol compositions with varying content of wa-  
 497 ter and sulfuric acid ( $\text{H}_2\text{SO}_4$ ). This results in an uncertainty of  $0.1 \mu\text{m}$ , with HT-HH par-  
 498 ticle effective radius ranging within  $0.4$ – $0.5 \mu\text{m}$  from March to July 2022, as also reported by  
 499 Duchamp et al. (2023), and hence in agreement with the aerosol size obtained from our anal-  
 500 ysis of AERONET data.

#### 501 4.2 A potential signature of volcanic ash in the coarse mode

502 Following the discussion on the size of the fine mode particles (Section 4.1), we discuss  
 503 further the coarse mode properties of the HT-HH plume during its first circumnavigation of  
 504 the globe. Indeed, based on size distributions, a secondary peak in the coarse mode is detected  
 505 by photometric data, possibly indicating the presence of coarse ash particles, albeit at an un-  
 506 known altitude.

507 Concurrently with the fine mode fingerprint of volcanic aerosols associated with the HT-  
 508 HH plume, a small excess in the coarse contribution to AOD, compared to background val-  
 509 ues, is observed at Lucinda (eastern Australia) in the days following the peak in AOD, from  
 510 17 to 23 January 2022 (Fig. 2b3 and S11b). Unfortunately, only 4 almucantar-derived aerosol  
 511 VSDs are available for that station at that time (Fig. S11c). These few VSDs nevertheless  
 512 indicate a slightly larger coarse mode, with an effective radius  $r_{eff}$  ranging in  $3.2$ – $3.3 \mu\text{m}$  on  
 513 late 16 January 2022, compared to measurements collected in the early morning of 16 Jan-  
 514 uary (before the HT-HH plume overpass) indicating a coarse mode  $r_{eff}$  of  $1.9 \mu\text{m}$  (Fig. S3.1).  
 515 Coarse particles on 16 January present a significantly larger size than coarse aerosols usually  
 516 observed at Lucinda, as shown by historical monthly-mean values ( $\pm 1\sigma$ ) at Lucinda which  
 517 range in  $1.6$ – $2.3 \mu\text{m}$  (blue shaded area in Fig. S3.1). When the tail of the HT-HH plume passes  
 518 over Lucinda four days later, on 20 January 2022,  $r_{eff}$  comes back down to  $2.0$ – $2.1 \mu\text{m}$ , hence

519 still remaining in the upper bound of commonly measured values for coarse aerosols at the  
520 station. Nevertheless, the coarse mode shape measured during HT-HH plume overpass is not  
521 statistically different from the coarse mode commonly measured at Lucinda, as shown by the  
522 climatological analysis of VSDs collected from 2009 to 2021 (selected with an Angstrom ex-  
523 ponent  $< 0.5$  to retain only abundant coarse particles, see dashed black line in Fig. S11c).  
524 We also note the absence of an unusual coarse mode (within the monthly-mean range) when  
525 the HT-HH plume passes a few days later over the station of Learmonth in western Australia  
526 (Fig. S3.2). Therefore, the volcanic origin of the coarse mode measured in Australia during  
527 HT-HH plume overpass remains inconclusive, as we cannot exclude that it originates from  
528 confounding non-volcanic sources, such as sea salts or desert dusts.

529 In contrast, at La Réunion, poorly-absorbing coarse particles with an unusually large  
530 size are recorded when the HT-HH plume passes over Maido OPAR, associated with  $r_{eff}$  of  
531  $4.6 \mu\text{m}$  on 22 January 2022 exceeding monthly values ranging in  $1.6\text{--}3.8 \mu\text{m}$  in January (Fig.  
532 S3.3). An enhanced coarse mode AOD is also detected at St-Denis Réunion station the same  
533 day (Fig. 2b3). Concurrently, ground-based LIDAR observations performed at Maido OPAR  
534 during the previous and following nights (respectively, 21-22 January and 22-23 January) de-  
535 tect thick and dense volcanic layers from HT-HH at an altitude between 27-30 km (21-22 Jan-  
536 uary) and 24-28 km (22-23 January), respectively (Baron et al., 2023; Khaykin et al., 2022).  
537 These layers present unusually large negative Angstrom exponents (of  $\approx -0.8$ ), indicating  
538 the significant presence of coarse particles (Baron et al., 2023). Therefore, both AERONET  
539 and LIDAR observations suggest the presence of coarse particles of volcanic origin over La  
540 Réunion on 22 January 2022.

541 Taken together, these observations are best explained by the presence of coarse ash par-  
542 ticles affected by sulfate coating, producing particles with sulfate-like absorbing properties,  
543 and traveling coevally with smaller sulfate aerosols. This volcanic signature in the coarse mode  
544 is observed only during the first HT-HH plume overpass at La Réunion (Maido OPAR) on  
545 22 January, and to a lesser extent in the younger plume at the Australian stations of Lucinda  
546 and Learmonth from 16 and 20 January.

547 The predominance of aerosols with low-depolarization properties measured with CALIOP  
548 after 15 January 2022 would be in agreement with this interpretation, as the coating of ash  
549 particles by sulfate likely leads to a spherical shape, especially for 7-day old particles at La  
550 Réunion. However, according to Legras et al. (2022) and Khaykin et al. (2022), these depo-  
551 larizing properties are carried by small particles, and ash is believed to have been “washed  
552 out within the first day following the eruption” (Legras et al., 2022). In reality, when trav-  
553 eling in a dense  $\text{SO}_2$ - and sulfate-rich environment, finer ash particles are likely to stealthily  
554 remain in suspension as sulfate-coated ash particles, making them hard to distinguish from  
555 more chemically-pristine sulfate droplets. Furthermore, spatial heterogeneity within the plume  
556 in the first days post-eruption may not be fully sampled by lidar transects. This is in keep-  
557 ing with the presence of two isolated plume parcels with depolarizing properties ( $>50\%$ ) in  
558 the 16 January 2023 CALIOP transect at an altitude in 26-28 km (Fig. S2). Determining with  
559 confidence the actual fate of sulfate-coated ash particles over a time-scale of the order of a  
560 week would require more observations, which are unfortunately lacking.

### 561 4.3 Comparison with Pinatubo eruption: contrasting aerosol growth rates

562 We document in our study the gas to particle conversion of sulfuric species in the HT-  
563 HH plume, with  $\text{SO}_2$  being oxidized to form stratospheric sulfuric acid aerosols. Their peak  
564 radius, quantified by analysis of photometric data, almost doubles from  $0.24 \mu\text{m}$  (eastern Aus-

565 tralia, Lucinda) to  $0.46 \mu\text{m}$  (La Réunion) in six days (Figures 2 and 5). An initial increase  
 566 of the aerosol size was already reported by Khaykin et al. (2022), albeit over a longer time  
 567 scale ( $\sim 1$  month), likely due to different spatio-temporal sampling and sensitivity. We also  
 568 show that HT-HH aerosols reach a relatively stable size with  $r_{peak}$  of  $0.35\text{--}0.45 \mu\text{m}$  less than  
 569 two weeks after eruption (Fig. 5). Aerosol size then remains stable at  $0.3\text{--}0.5 \mu\text{m}$ , with a mean  
 570 value around  $0.4 \mu\text{m}$  over the 1.3 years after eruption (Fig. 8b).

571 Given the importance of aerosol size in the climate impact of large volcanic eruptions,  
 572 we aim at comparing the evolution in time of HT-HH aerosol size with the 1991 Pinatubo erup-  
 573 tion (VEI 6). Unfortunately, lack of AERONET data prior to mid-1993 (birth of the network)  
 574 prevents the application of the same methodology to retrieve Pinatubo aerosol (peak) radii  
 575 in the two years after eruption. For this period of time, Russell et al. (1996) compiled a large  
 576 variety of in situ and remote measurements allowing for describing the evolution of Pinatubo  
 577 aerosol effective radius until August 1993 (Fig. 8c), in agreement with other ground-based  
 578 spectral extinction observations later gathered by (Stothers, 2001). Two years after eruption,  
 579 a middle mode peak associated with  $r_{eff}$  of  $0.56 \mu\text{m}$  was highlighted from observations at  
 580 two AERONET stations in the USA and Brazil in June 1993 (B. Holben et al., 1996; T. F. Eck  
 581 et al., 2010), in agreement with retrievals from spectral AOD at a single Japanese station from  
 582 January to April 1992 (Asano et al., 1993). Extending these early works, we perform retro-  
 583 spectively a more exhaustive analysis of AERONET data at four stations in the USA and Brazil  
 584 (GSFC, Seville, Cuiaba and Brasilia) to evaluate Pinatubo aerosol size evolution in 1993–  
 585 1994 (Fig. 8c). We overlay our results with the synthesis of Russell et al. (1996) (Fig. 8d).

586 The short temporal overlap between Russell et al. (1996) and our results at +2 years  
 587 after eruption shows an agreement on Pinatubo aerosol radius ( $\sim 0.5 \mu\text{m}$ ) (Fig. 8c). In ad-  
 588 dition, the decreasing trend in Pinatubo aerosol size visible in our AERONET analysis for  
 589 1993–1995 is consistent with the time evolution of Pinatubo radius over the period 1991–1993  
 590 by Russell et al. (1996) (Fig. 8d). As a side remark, this agreement also implies that, within  
 591 the scope of our analysis, AERONET-derived peak radius  $r_{peak}$  can be compared, in good  
 592 approximation, with the effective radius derived from other techniques, such as in-situ mea-  
 593 surements.

594 First-order conclusions can be raised from this comparison regarding the early aerosol  
 595 growth rate and the year-long evolution of stratospheric aerosols. First, the timescale of strato-  
 596 spheric aerosol growth appears much longer following the June 1991 Pinatubo eruption com-  
 597 pared to the HT-HH case. According to Russell et al. (1996),  $r_{eff}$  grew from around  $0.2\text{--}0.3$   
 598  $\mu\text{m}$  in late 1991, up to  $0.5\text{--}0.6 \mu\text{m}$  over the timescale of one year (Fig. 8c). Hence, it took about  
 599 3–4 months for the Pinatubo aerosols to reach the size reached by HT-HH aerosols in just  
 600 a couple of weeks ( $0.4 \mu\text{m}$ ).

601 Fast growth rate of HT-HH sulfate aerosols could be linked to the strong water com-  
 602 ponent of the plume resulting from exceptionally powerful water-magma interactions during  
 603 the eruption, which was comparatively limited during the 1991 Pinatubo eruption. This mas-  
 604 sive release of water is attested by satellite observations of an exceptional hydration of the  
 605 stratosphere (Millan et al., 2022; Vömel et al., 2022). This input of water is expected to in-  
 606 crease the level of hydroxyl OH-radicals, leading to faster oxidation of  $\text{SO}_2$  (Pinto et al., 1989;  
 607 Bekki, 1995; Zhu et al., 2022). Then, in the accumulation mode ( $>0.1 \mu\text{m}$ ), aerosols grow by  
 608 coagulation and by condensation of vapor onto existing particles (Seinfeld & Pandis, 2012;  
 609 Kremser et al., 2016). Overall, the presence of excess water may have enhanced the positive  
 610 feedback between an early formation of sulfuric acid, coagulation and condensation, leading  
 611 to a faster aerosol growth rate of HT-HH aerosols.

612 Model simulations with large stratospheric water vapour input, compared to simulations  
613 that do not account for a large water abundance, show that the HT-HH SO<sub>2</sub> lifetime is halved,  
614 down to 12 days (Zhu et al., 2022). This timescale is comparable with our observed stabi-  
615 lization of aerosol radius during the first circumnavigation. Likewise, model simulations show  
616 an increase in  $r_{eff}$ , ranging from 0.2 to 0.35  $\mu\text{m}$  or more, early February 2022, at 36 hPa ( $\approx$  21  
617 km) (Zhu et al., 2022), a size consistent with our observations.

618 Apart from the available sulfur dioxide and water vapour budgets, the altitude of a vol-  
619 canic plume is another important factor controlling the growth rate of aerosols (Bauman et  
620 al., 2003; Ansmann et al., 1997; Sioris et al., 2010). Besides, the massive release of water by  
621 the HT-HH eruption had specific effects on the dynamics of the plume that could, in turn,  
622 influence the evolution of the physico-chemical environment of these aerosols. For instance,  
623 both aerosols and water vapour descended together by 4 to 6 km until early February 2022  
624 due to the cooling effect of water vapour, and then separated vertically as aerosols sedimented  
625 and water vapour ascended (Sellitto et al., 2022; Schoeberl et al., 2022; Legras et al., 2022).  
626 The initial cooling and descent have likely played a role in the accelerated formation of the  
627 sulfates.

628 A second conclusion concerns the size of the aerosols after the growth phase. In spite  
629 of a slower growth compared to HT-HH, our comparison shows that Pinatubo aerosols grew  
630 steadily over the course of about one year until reaching their maximum size of  $\sim$  0.5–0.6  $\mu\text{m}$ .  
631 Hence, from + 4 months after eruption, Pinatubo aerosols are larger than HT-HH aerosols,  
632 until at least +1.3 year post-eruption (at the time of writing) (Fig. 8d). For Pinatubo, af-  
633 ter reaching their maximum size, aerosol size started to decrease (Russell et al., 1996). In the  
634 1993-1995 interval of time (+2-3 yrs after eruption), our analysis of AERONET observations  
635 indicates that Pinatubo particle peak radius further decrease from  $\sim$  0.50 down to  $\sim$  0.35  $\mu\text{m}$ .  
636 This systematic decrease in aerosol size likely results from sedimentation of the fraction of  
637 larger particles in the population, whose signature had previously been outweighed by aerosol  
638 condensation and coagulation (Russell et al., 1996). In contrast, for HT-HH, we note that,  
639 after a transient homogenization phase lasting  $\sim$  4 months, the amplitude of the HT-HH vol-  
640 canic mode in VSDs remains relatively stable and homogeneous over the southern hemisphere  
641 (Fig. 8a). Coevally, the aerosol size does not show any clear, systematic and monotonous de-  
642 cay (at the time of writing) (Fig. 8b). This observation does not appear to match a scenario  
643 involving a fast decay of HT-HH aerosols. Nevertheless, despite being smaller than Pinatubo  
644 sulfate aerosols, HT-HH particles are still larger than for other recent stratospheric eruptions  
645 such as 2009 Sarychev (Kuril Islands) and 2008 Kasatochi (Aleutian Islands), with  $r_{eff}$  rang-  
646 ing in 0.15–0.30  $\mu\text{m}$  in the three months post-eruption from balloon-borne experiments (Jégou  
647 et al., 2013) and sunphotometric observations at polar stations (N. T. O’Neill et al., 2012).  
648 An even smaller effective radius of 0.16  $\mu\text{m}$  is reported for 2008 Kasatochi aerosols one month  
649 post-eruption from LIDAR observations (Hoffmann et al., 2010). The consequences of these  
650 contrasting aerosol microphysical behaviours on climate need to be examined.

## 651 5 Conclusions and perspectives

652 Uncertainty on the size distribution of stratospheric sulfate aerosols, a fundamental pa-  
653 rameter for modeling the climate response to eruptions, affects modeled aerosol optical depth  
654 and lifetime of stratospheric aerosols (Haywood et al., 2010; Kravitz et al., 2011; Dhomse et  
655 al., 2014; Lurton et al., 2018), and may explain inaccurate evaluation of the volcanic forcing  
656 and the mismatch between simulated and observed temperature anomalies (Timmreck et al.,  
657 2010; Mann et al., 2015; Kremser et al., 2016). Narrowing down these uncertainties is essen-



658 tial to better predict the formation and growth of HT-HH sulfate aerosols, especially given  
659 the excess stratospheric water vapour conditions that prevailed after the Hunga Tonga erup-  
660 tion (Zhu et al., 2022). Furthermore, water vapour also has a radiative effect on its own, that  
661 may produce a slightly positive net warming of the atmosphere, hence opposite to the expected  
662 effect of sulfate aerosols alone (Sellitto et al., 2022; Jenkins et al., 2023). On the other hand,  
663 failing to account for sulfate aerosols in chemistry-climate model simulations would lead to  
664 a weakened polar vortex and an enhanced Brewer-Dobson Circulation (Wang et al., 2022).  
665 Accordingly, since the forcings from both sulfate aerosols and water components need to be  
666 jointly considered (Wang et al., 2022; Zhu et al., 2022), constraining aerosol size is essential  
667 to assess the net effect of the eruption on planetary radiative balance.

668 Contrary to spaceborne occultation/limb-scattering measurements (Wrana et al., 2021;  
669 Thomason et al., 2021; Taha et al., 2021; Khaykin et al., 2022), AERONET inversions present  
670 the advantage of not requiring any a priori assumption on particle size distribution or chem-  
671 ical composition for the retrieval of volume size distribution. Together with satellite obser-  
672 vations, exhaustive analysis of photometric observations from the AERONET network allows  
673 us to track the size of HT-HH sulfate aerosols with time. Despite a remarkably rapid growth  
674 rate in the week after eruption, we show that HT-HH sulfate particles remain smaller than  
675 Pinatubo aerosols 1.3 years after eruption. For a fixed mass, smaller-size stratospheric aerosols  
676 have a greater climate impact than larger aerosols. Smaller particles scatter visible light more  
677 efficiently and will sediment at lower rate, implying a larger and longer-lasting tropospheric  
678 cooling (Pinto et al., 1989; Bauman et al., 2003; Timmreck et al., 2009; Kremser et al., 2016).  
679 Furthermore, ozone destruction is enhanced by smaller aerosols via heterogeneous stratospheric  
680 chemistry (Solomon, 1999; Tilmes et al., 2008) and chemistry-climate model simulations have  
681 already shown that HT-HH aerosols would enhance polar ozone loss (Wang et al., 2022). The  
682 cause of the peculiar microphysical properties of HT-HH aerosols might be traced back to strong  
683 magma-water interactions during the eruption. Yet, geological markers of pre-historical un-  
684 derwater eruptions are difficult to identify and their climate impact may have been overlooked.

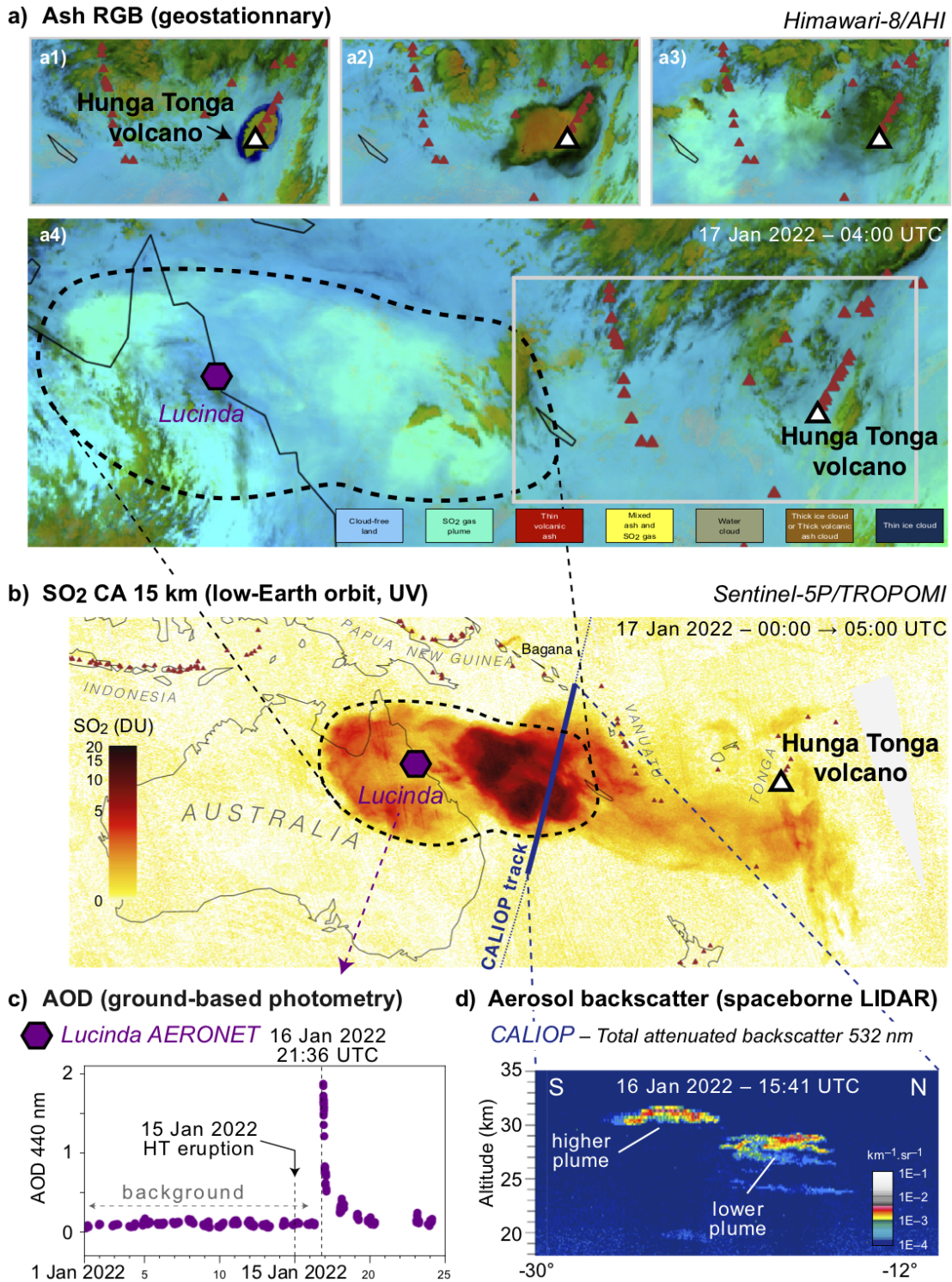
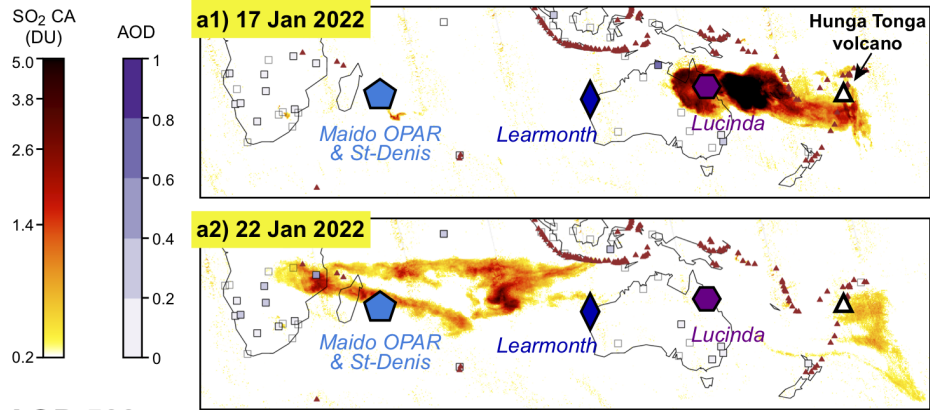
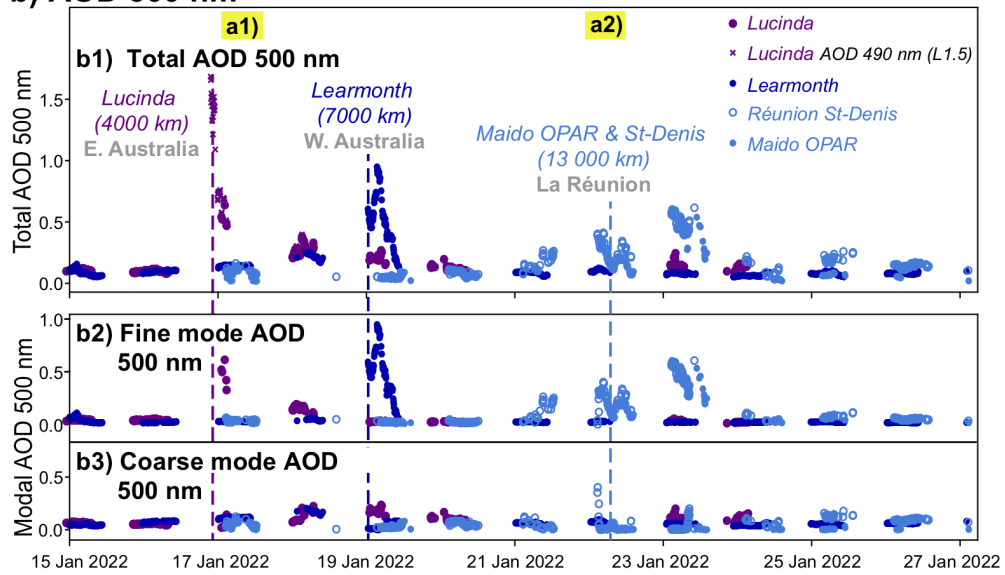


**Figure 1.** (a) Ash RGB products from HIMAWARI-8/AHI satellite observations of the near-source HT-HH plume from 15 January 2022 05:00 UTC to the time of TROPOMI acquisition detecting the dispersed plume over Australia (17 January 2022, 04:00 UTC). Grey rectangle in a4 shows extent of panels a1 to a3. Black triangle shows location of HT-HH volcano. Red triangles are other active volcanoes. (b) SO<sub>2</sub>-rich plume from TROPOMI (15 km product) on 17 January (between 00:00 and 05:00 UTC) with indication of the track of CALIOP spaceborne LIDAR night-time observations (dark blue line) crossing the plume ≈10 hours before TROPOMI acquisition, and of the location of the AERONET ground station of Lucinda in eastern Australia (white square). (c) AOD<sub>440nm</sub> L1.5 values observed at Lucinda in January 2022 until the arrival of HT-HH aerosols on 16 January 2022. (d) Total attenuated backscatter signal (at 532 nm) with altitude along the portion of the CALIOP track detecting HT-HH aerosols (16 January 2022, 15:41 UTC, latitudes ranging in -30° to -12°).

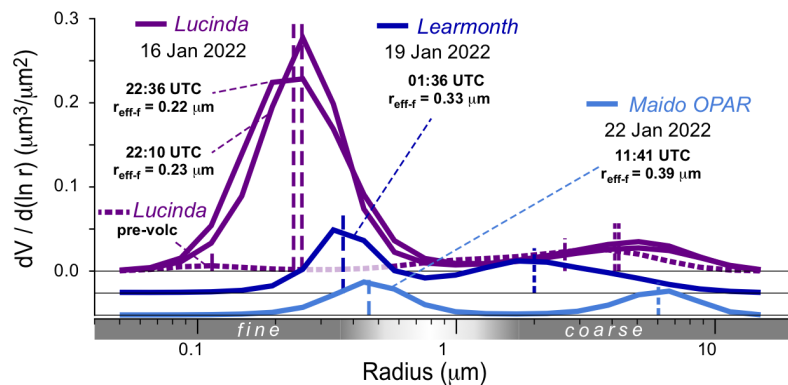
**a) SO<sub>2</sub> CA (TROPOMI)**



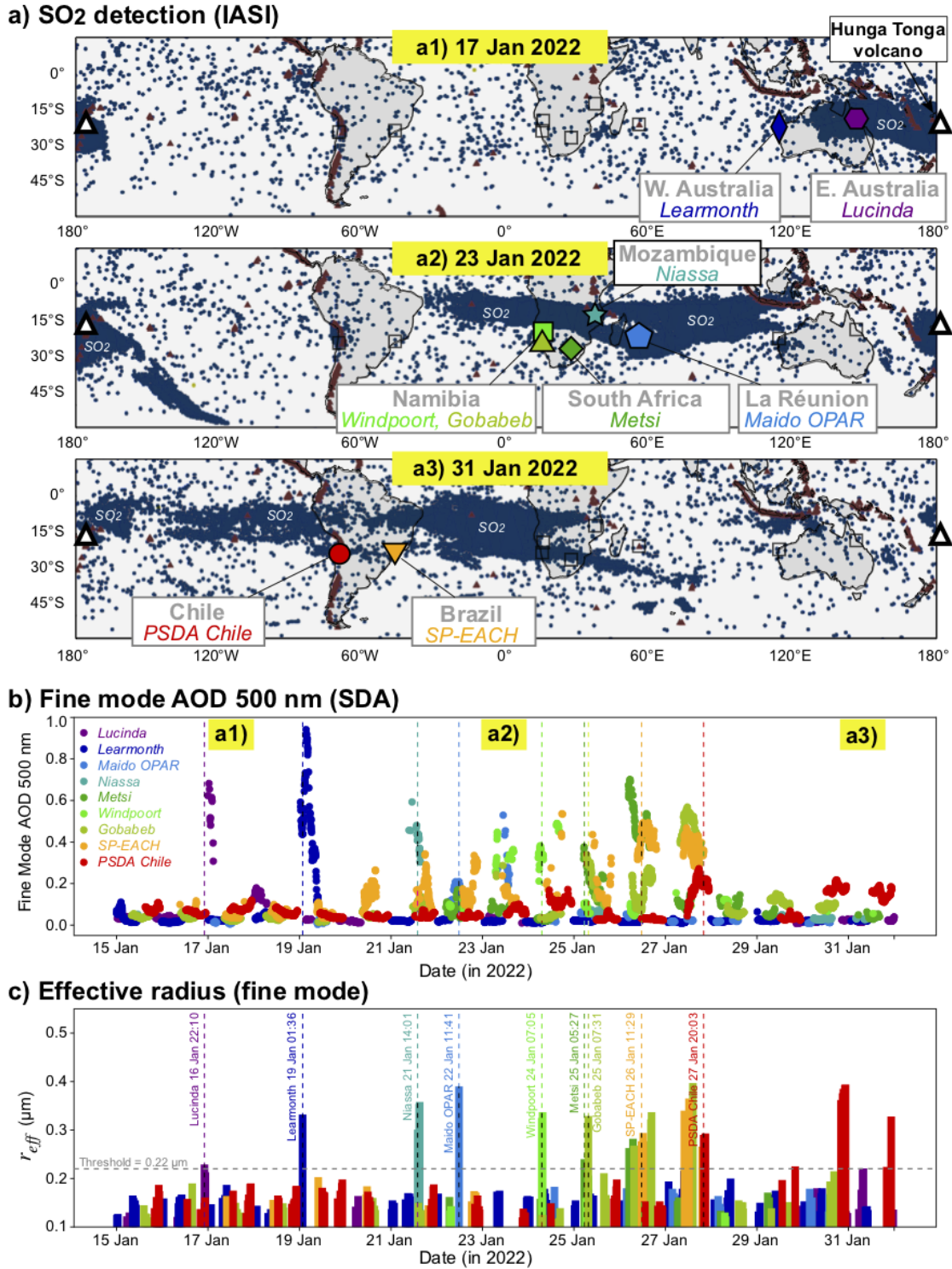
**b) AOD 500 nm**



**c) Aerosol volume size distribution**

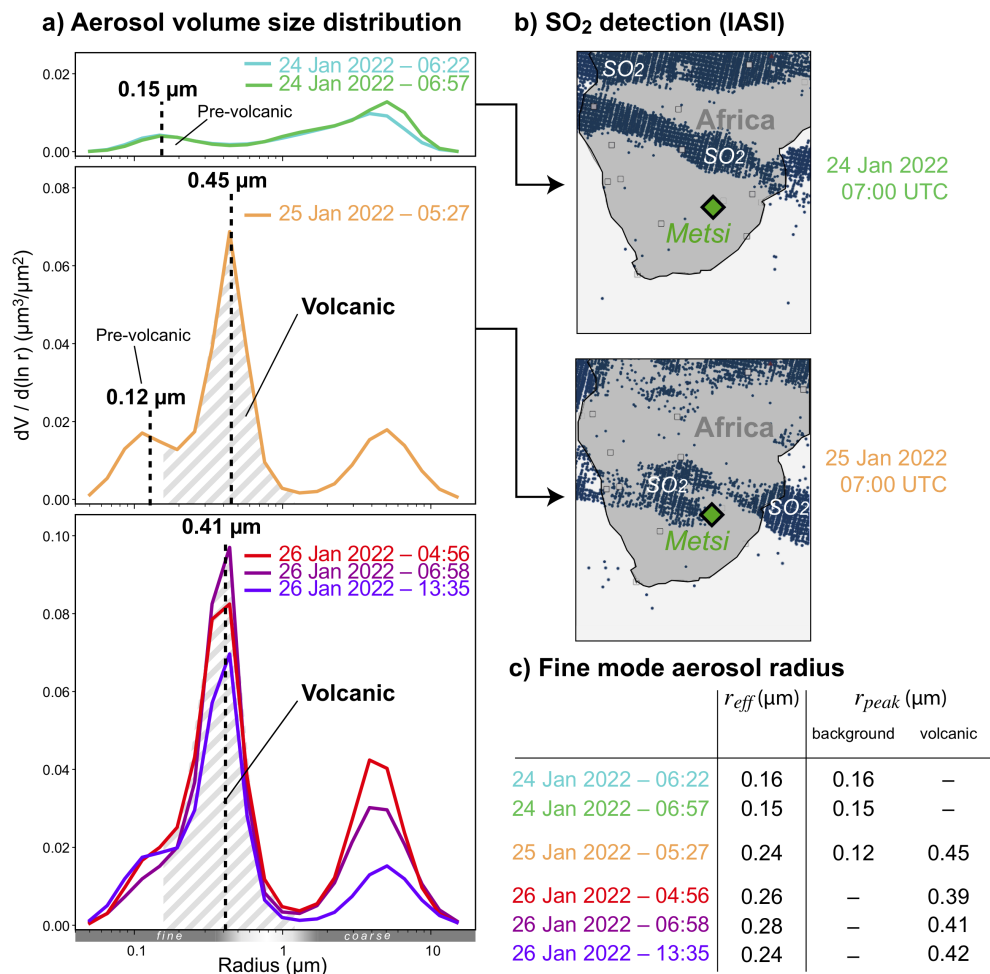


**Figure 2.** (a) HT-HH SO<sub>2</sub>-rich plume from Sentinel-5P/TROPOMI column amount observations (15 km product) on (a1) 17 and (a2) 22 January 2022, with indication of the AERONET stations (squares colored according to daily mean AOD<sub>440±18</sub>) of Lucinda (eastern Australia, purple), Learmonth (western Australia, dark blue), Mairo OPAR (sky blue, solid circles) and St-Denis (sky blue, circles) (both on Réunion Island), respectively at 4000, 7000 and 13000 km from the volcanic source. (b) Time series of (b1) total, (b2) fine and (b3) coarse mode AOD<sub>500nm</sub> (SDA algorithm) from L1.5 direct sun observations (circles). Note that the plot is complemented with L1.5 total AOD observations at 490 nm (crosses) for Lucinda, which provide a better temporal coverage. (c) Aerosol volume size distribution derived from almucantar observations (date indicated by vertical dashed lines in (b)) first available after the arrival of the HT-HH plume at the stations (vertical dashed lines indicate  $r_{peak}$  in both fine/coarse modes).

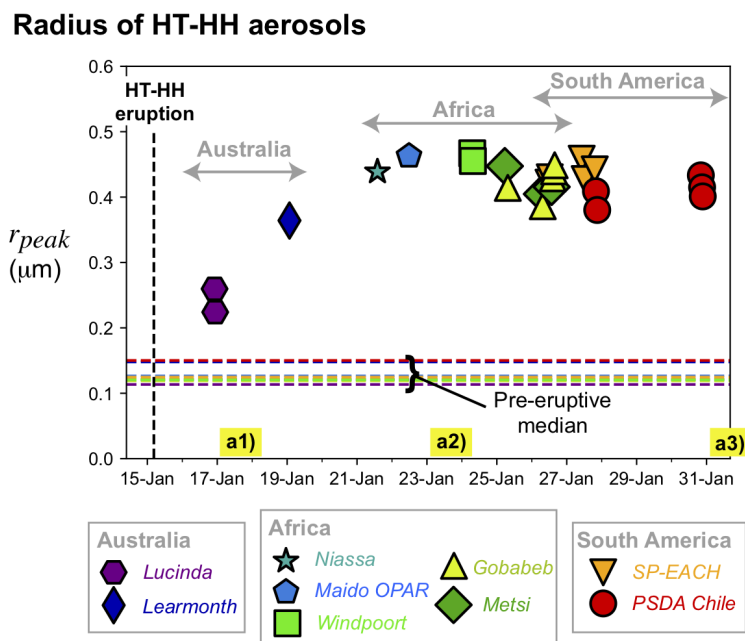


**Figure 3.** (a) Transport and dispersion of the HT-HH SO<sub>2</sub> plume during first circumnavigation around the globe. Blue dots show SO<sub>2</sub> detection from MetOp-B and -C/IASI AM and PM observations, retrieved from SO<sub>2</sub> height products, on (a1) 17, (a2) 23 and (a3) 31 January 2022. Symbols indicate the location of ground-based AERONET photometric observations displayed in (b) and (c) with colors varying with longitude. (b) Fine mode AOD<sub>500 nm</sub> (SDA algorithm) from direct sun measurements. (c) Fine mode effective radius from almucantar observations. Vertical dashed lines indicate, for each of the stations, the time of first detection of HT-HH aerosols (defined as particles with a fine mode  $r_{eff} > 0.22 \mu\text{m}$ .)

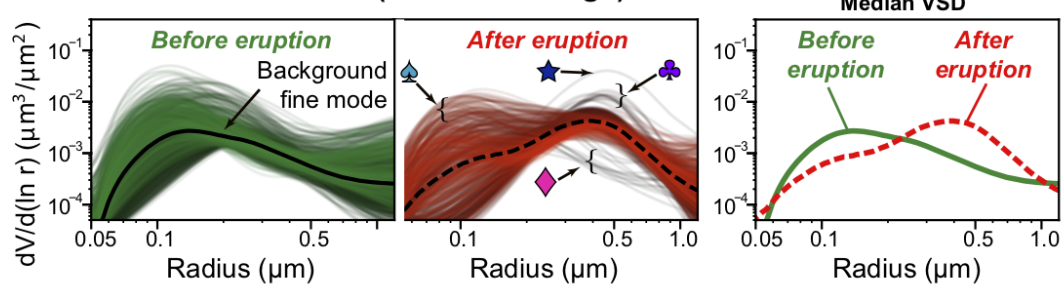
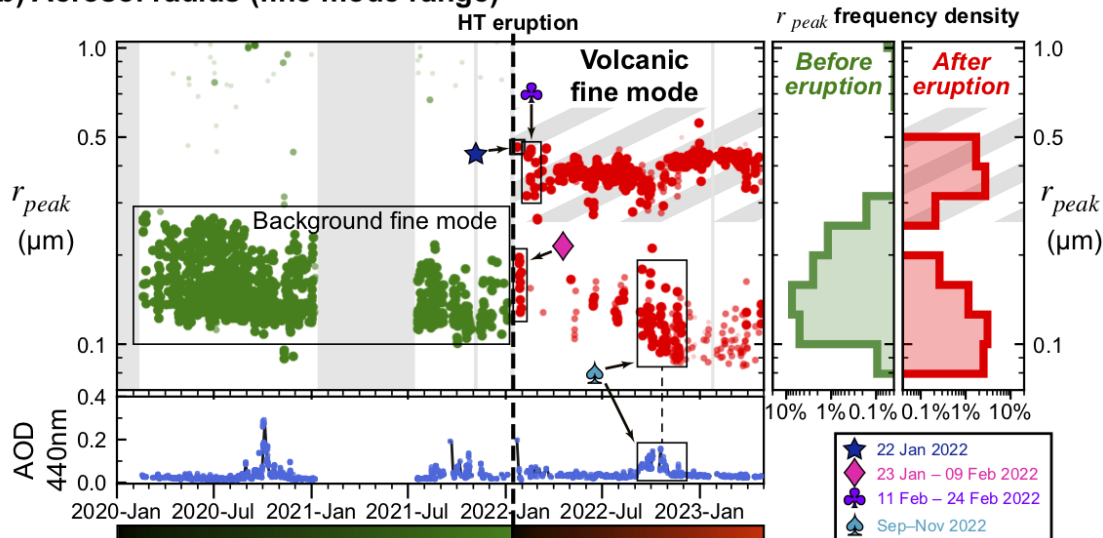
◆ *Metsi*



**Figure 4.** Detection of volcanic aerosols at Metsi AERONET station (South Africa) at the time of first overpass by the HT-HH plume. (a) Aerosol VSD on (top) 24 January 2022 (background or pre-volcanic), (middle) 25 and (bottom) 26 January 2022 (impacted by HT-HH), with indication in bold of radii ( $r_{peak}$ ) of local maxima of the VSD identified with a spline interpolation. (b) Detection of the HT-HH SO<sub>2</sub> plume using MetOp-B and -C/IASI SO<sub>2</sub> height product on (top) 24 and (bottom) 25 January AM (~ 07:00 UTC) with the location of Metsi station indicated by a green diamond. (c) Table of AERONET-derived particle size in the fine range ( $\mu\text{m}$ ): fine mode effective radius ( $r_{eff}$ , left) and peak radius ( $r_{peak}$ , right). For  $r_{peak}$ , background and volcanic aerosol radii may be estimated simultaneously, and are distinguished in two separate columns.



**Figure 5.** HT-HH aerosol peak radius during first circumnavigation of the globe (January 2022), at selected AERONET stations in three different continents indicated by colored symbols ( $\text{AOD}_{440\text{nm}} > 0.1$ ). This size corresponds to the radius of the aerosols giving the largest contribution to the volume size distribution in the fine range ( $r_{peak,1}$ ). Horizontal dashed lines indicate the median of  $r_{peak,1}$  in the fine mode between 1 January 2020 and 15 January 2022 (date of the eruption) for each station. Vertical dashed line marks the time of the HT-HH eruption. Annotations (a1) 17 Jan, (a2) 23 Jan and (a3) 31 Jan 2022 refer to the time of IASI  $\text{SO}_2$  detections in Fig. 3. VSDs associated to each datapoint are shown in Fig. S5.

 **Maido OPAR**
**a) Volume size distributions (fine mode range)****b) Aerosol radius (fine mode range)**

**Figure 6.** Aerosol size over La Réunion island/Maido OPAR station ( $21^{\circ}\text{S}$ ) from January 2020 to May 2023. (a) VSDs displayed in the fine mode range before (left, green) and after (middle, red) the HT-HH eruption, for the subset of VSDs with  $r_{peak,1} < 0.90 \mu\text{m}$  or  $r_{peak,2} < 0.90 \mu\text{m}$  (ie. those including either their largest or second-largest peak in the fine mode range). Color coding varies with time, as indicated by the colorscale at the bottom of the figure. Thick black lines show the median of the VSDs, which are duplicated in the right panel to facilitate comparison. (b) Aerosol peak radius in the fine mode range. Eruption date is indicated by a vertical dashed line. Left panel: time series of radii  $r_{peak,i}$  associated to local maxima in the spline interpolation of the aerosol VSD. The three largest local maxima ( $r_{peak,i}$ , with  $i=1,2,3$ ) are ordered from largest to lowest volume abundances and displayed with symbols of decreasing size and opacity. Grey areas indicate data gaps longer than 15 days. Right panel: frequency density histograms of  $r_{peak}$  before/after eruption. Symbols highlight detections of special interest, discussed in the text ( $\star$ : first plume overpass on 22 Jan 2022;  $\blacklozenge$ : temporary lull during first circumnavigation;  $\clubsuit$ : resumption of the volcanic signal during second overpass and continued detection thereafter;  $\spadesuit$ : increased background fine mode due to biomass burning). The full distribution of  $r_{peak}$ , including the coarse mode range, is illustrated in Fig. S8b.

**Aerosol radius (fine mode range)**

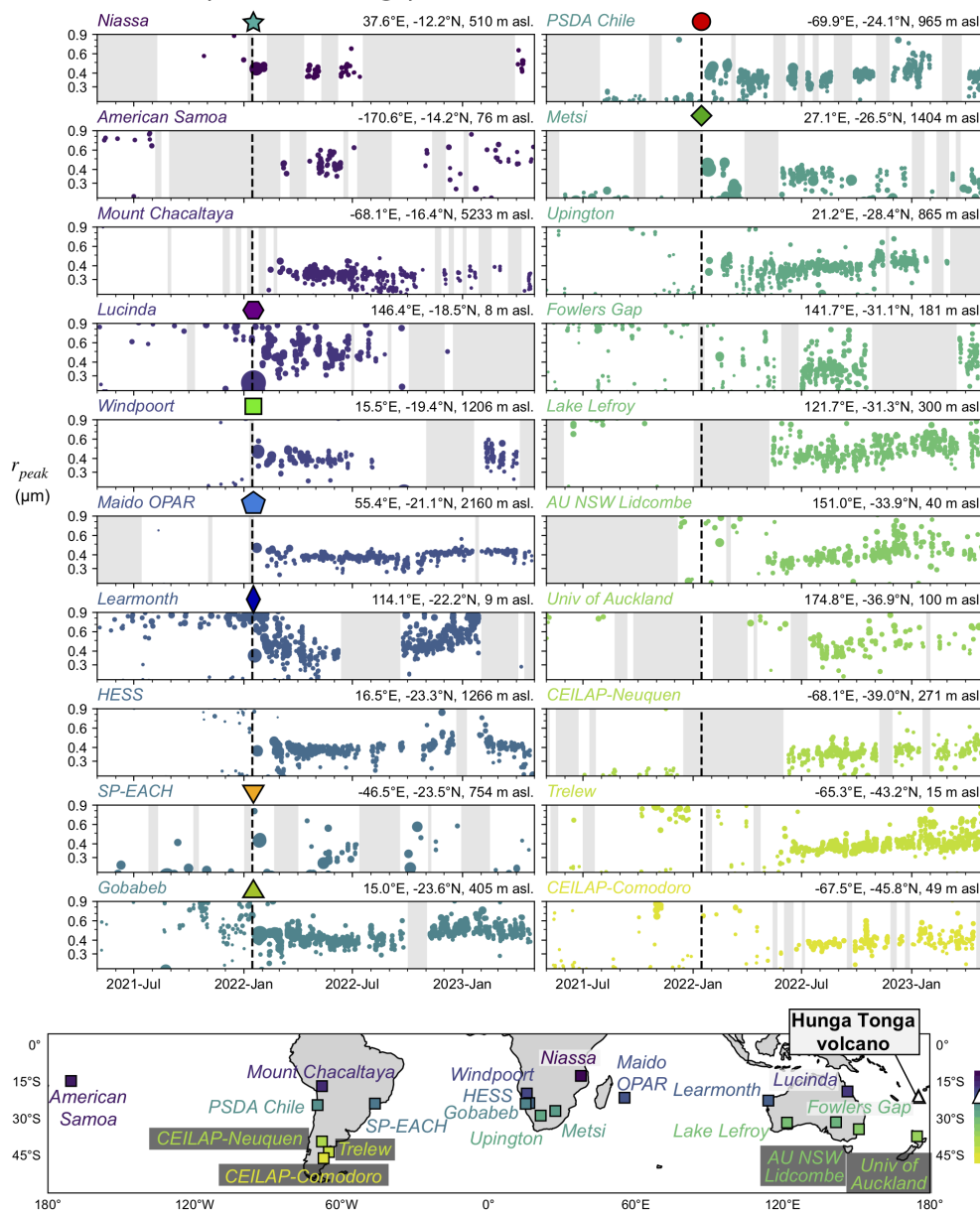
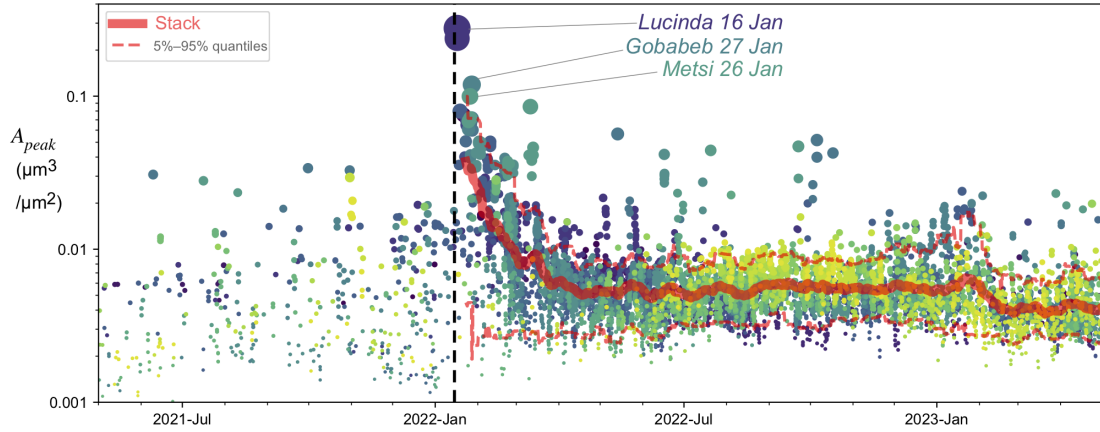


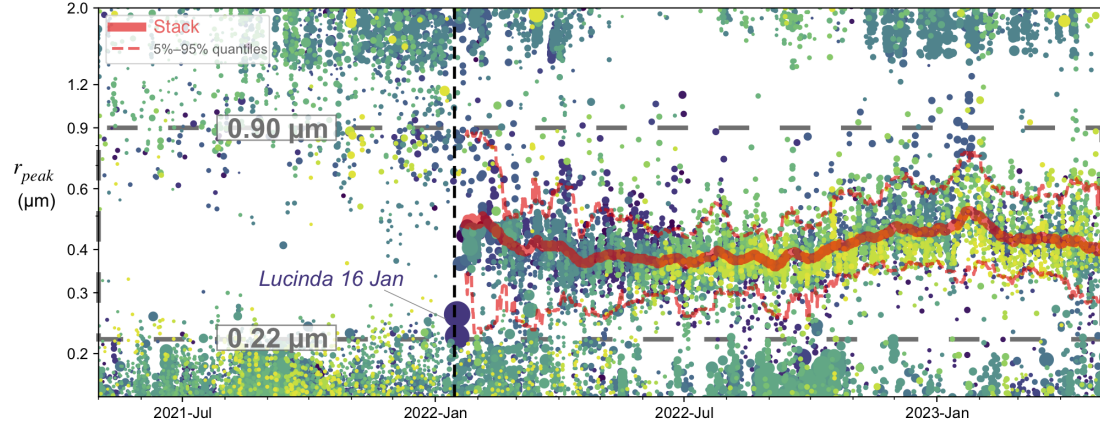
**Figure 7.** Aerosol peak radius  $r_{peak}$  associated to the HT-HH volcanic fine mode (plotted in the 0.22-0.90  $\mu\text{m}$  range), from May 2021 to May 2023, at 20 AERONET stations of the southern hemisphere. To avoid clutter, only the largest and second-largest peaks of each VSD are plotted (ie.,  $r_{peak,1}$  and  $r_{peak,2}$ ), with symbol size proportional to VSD amplitude at the peak (ie.,  $A_{peak,1}$  and  $A_{peak,2}$ , respectively). The color of station symbol varies with latitude, as shown in the map in the bottom panel. Grey areas indicate data gaps longer than 15 days. Aerosol  $r_{peak}$  values covering the whole size range (fine and coarse modes) are illustrated for each station in Fig. S7 to S9. HT-HH eruption is indicated by dashed vertical line. The symbols of the nine stations discussed in Section 3.1.2 are recalled at the top of each sub-panel.



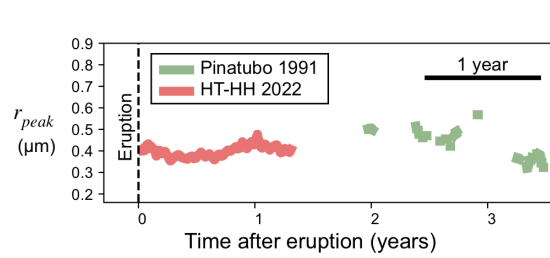
**a) Peak amplitude of VSD in volcanic fine mode range [0.22–0.90]  $\mu\text{m}$**



**b) Radius of volcanic fine mode**



**c) Comparison with Pinatubo eruption**



**d) Pinatubo effective radius (after Russell et al., 1996)**

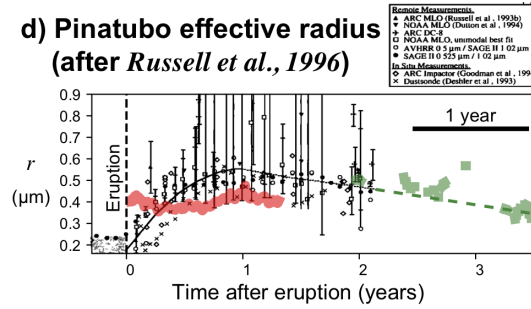


**Figure 8.** (a) Stack of the time-series of aerosol peak amplitudes  $A_{peak}$  for the largest and second-largest peaks situated within the volcanic size range (ie.,  $A_{peak,1}$ , if  $r_{peak,1} \in [0.22 - 0.90] \mu\text{m}$ , and  $A_{peak,2}$ , if  $r_{peak,2} \in [0.22 - 0.90] \mu\text{m}$ ) at the 20 stations of the southern hemisphere shown in Fig. 7. (b) Stack of the time-series of aerosol peak radius  $r_{peak,i}$  (with  $i=1,2$ ). In (a) and (b), the thick red line is the rolling median computed after the HT-HH eruption (vertical dashed line) with a window size of 15 days, restricted to data points falling within the volcanic size range. Dashed red lines are the 5% and 95% quantiles. Symbol size is proportional to  $A_{peak}$ , while colors depend on station latitude, as in Fig. 7. (c) Temporal evolution of aerosol radius based on the analysis of AERONET data for HT-HH (red, same as in (b)) and Pinatubo (green) until + 1300 days post-eruption. The analysis of AERONET data for Pinatubo 1991 was conducted using the same methodology as for HT-HH, albeit with a more limited dataset (first data point: mid-1993). See Figure S12 for details of the analysis of the Pinatubo 1991 particles. (d) Same as (c), overlaid on the effective radius of Pinatubo aerosols from Fig. 4 in the compilation by Russell et al. (1996), filling the gap of AERONET data in the 1991–1993 interval. Green dashed line is the prolongation of the mid-1992-to-mid-1993 trend of Russell et al. (1996).

## Open Research Section

All data used in this study are publicly available:

- Facilities of the European Space Agency (ESA) were used for access to Sentinel-5P TROPOMI Level 2 SO<sub>2</sub> products (ESA Copernicus, 2020)
- Facilities of EUMETSAT SAF on Atmospheric Composition Monitoring (<http://ac-saf.eumetsat.int>) were used for access to MetOp-B and MetOp-C/IASI L2 column amount products (EUMETSAT, 2018)
- The IASI portal of the AERIS Data and Services Center (<https://iasi.aeris-data.fr>) was used for access to MetOp-B and MetOp-C IASI L2 columns and altitude products (Clarisse, 2013, 2019)
- The Data Integration and Analysis System (DIAS) by Japan Agency for Marine-Earth Science and Technology (JAMSTEC) was used for access to Himawari-8 Level 1B products (Japan Meteorological Agency, 2015)
- Facilities of NASA-LARC (<https://www-calipso.larc.nasa.gov/>) were used for access to CALIPSO-CALIOP Level 1B products (NASA/CNES/LARC/SD/ASDC, 2022)
- Facilities of NASA-GSFC ([https://aeronet.gsfc.nasa.gov/cgi-bin/webtool\\_inv\\_v3](https://aeronet.gsfc.nasa.gov/cgi-bin/webtool_inv_v3)) were used for access to AERONET Level 1.5 products (AERONET Federation, 1993)

The VOLCPLUME web-based portal, freely, accessible via <https://volcplume.aeris-data.fr>, and hosted by AERIS/ICARE Data and Services Center (<https://www.icare.univ-lille.fr/data-policy/?policy=icare>) was used for satellite and ground-based multi-station analysis (Boichu & Mathurin, 2022).

## Acknowledgments

Support from AERIS/ICARE Data and Services centre, for the co-development of the VOLCPLUME web portal (<https://doi.org/10.25326/362>), and Horizon Europe FAIR-EASE project (grant No. 101058785) are acknowledged. This work is a contribution to the CaPPA project (ANR-11-LABX-0005-01) funded by ANR, Hauts-de-France Region and FEDER. AERONET staff is thanked for calibrating and maintaining instrumentation of the network as well as data processing. We warmly thank the site managers: V. Dufflot (Maido OPAR, Réunion St-Denis), T. Schroeder (Lucinda), I. Lau (Learmonth), A. Queface (Niassa), P. Gupta (Metsi), K. Negussie (Windpoort), S. Piketh (Gobabeb), A. Marzo (PSDA Chile) and M. Yamasoe (SP-EACH). We acknowledge the French component of AERONET operating within the Center for Aerosol Remote sensing (CARS) of the ACTRIS Atmospheric Research Infrastructure.

We thank four anonymous reviewers for their insightful comments.

## References

- AERONET Federation. (1993). *Aerosol RObotic NETwork (AERONET) Level 1.5 aerosol products, V3* [Dataset]. Retrieved from [https://aeronet.gsfc.nasa.gov/new\\_web/data\\_description.html](https://aeronet.gsfc.nasa.gov/new_web/data_description.html)
- Ansmann, A., Mattis, I., Wandinger, U., Wagner, F., Reichardt, J., & Dethler, T. (1997). Evolution of the Pinatubo aerosol: Raman lidar observations of particle optical depth, effective radius, mass, and surface area over Central Europe at 53.4 N. *Jour-*

- 726 *nal of the atmospheric sciences*, 54(22), 2630–2641.
- 727 Asano, S., Uchiyama, A., & Shiobara, M. (1993). NOTES AND CORRESPONDENCE:  
728 Spectral Optical Thickness and Size Distribution of the Pinatubo Volcanic Aerosols  
729 as Estimated by Ground-Based Sunphotometry. *Journal of the Meteorological*  
730 *Society of Japan. Ser. II*, 71(1), 165–173.
- 731 Baron, A., Chazette, P., Khaykin, S., Payen, G., Marquestaut, N., Bègue, N., & Duflo,  
732 V. (2023). Early Evolution of the Stratospheric Aerosol Plume Following the 2022  
733 Hunga Tonga-Hunga Ha’apai Eruption: Lidar Observations From Reunion (21° S,  
734 55° E). *Geophysical Research Letters*, 50(10), e2022GL101751.
- 735 Barreto, Á., A.E., C., Granados-Muñoz, M., Alados-Arboledas, L., Romero Campos, P.,  
736 Gröbner, J., ... others (2016). The new sun-sky-lunar Cimel CE318-T multiband  
737 photometer – a comprehensive performance evaluation. *Atmospheric Measurement*  
738 *Techniques*, 9(2), 631–654.
- 739 Bauman, J., Russell, P., Geller, M., & Hamill, P. (2003). A stratospheric aerosol cli-  
740 matology from SAGE II and CLAES measurements: 2. Results and comparisons,  
741 1984–1999. *Journal of Geophysical Research: Atmospheres*, 108(D13).
- 742 Bekki, S. (1995). Oxidation of volcanic SO<sub>2</sub>: a sink for stratospheric OH and H<sub>2</sub>O. *Geo-*  
743 *physical Research Letters*, 22(8), 913–916.
- 744 Bluth, G. J., Doiron, S. D., Schnetzler, C. C., Krueger, A. J., & Walter, L. S. (1992).  
745 Global tracking of the SO<sub>2</sub> clouds from the June, 1991 Mount Pinatubo eruptions.  
746 *Geophysical Research Letters*, 19(2), 151–154.
- 747 Boichu, M., & Mathurin, T. (2022). *VOLCPLUME, an interactive web portal for the*  
748 *multiscale analysis of volcanic plume physico-chemical properties* [Interactive Web-  
749 based Ressource]. Direct access: <https://volcplume.aeris-data.fr>. Retrieved August  
750 2023, from <https://www.icare.univ-lille.fr/volcplume/> doi: 10.25326/362
- 751 Bourassa, A. E., Zawada, D. J., Rieger, L. A., Warnock, T. W., Toohey, M., & Degen-  
752 stein, D. A. (2023). Tomographic Retrievals of Hunga Tonga-Hunga Ha’apai  
753 Volcanic Aerosol. *Geophysical Research Letters*, 50(3), e2022GL101978.
- 754 Carn, S., Krotkov, N., Fisher, B., & Li, C. (2022). Out of the blue: Volcanic SO<sub>2</sub> emis-  
755 sions during the 2021–2022 eruptions of Hunga Tonga—Hunga Ha’apai (Tonga).  
756 *Frontiers in Earth Science*, 10, 976962.
- 757 Carr, J. L., Horváth, Á., Wu, D. L., & Friberg, M. D. (2022). Stereo Plume Height and  
758 Motion Retrievals for the Record-Setting Hunga Tonga-Hunga Ha’apai Eruption of  
759 15 January 2022. *Geophysical Research Letters*, 49(9), e2022GL098131.
- 760 Clain, G., Baray, J.-L., Delmas, R., Diab, R., Leclair de Bellevue, J., Keckhut, P., ...  
761 Cammas, J.-P. (2009). Tropospheric ozone climatology at two Southern Hemi-  
762 sphere tropical/subtropical sites, (Reunion Island and Irene, South Africa) from  
763 ozonesondes, LIDAR, and in situ aircraft measurements. *Atmospheric Chemistry*  
764 *and Physics*, 9(5), 1723–1734.
- 765 Clarisse, L. (2013). *MetOp-B IASI Level 2 Sulphur Dioxide Total Column and Altitude.*  
766 *V2.1.0* [Dataset]. Retrieved from [https://www.aeris-data.fr/en/landing-page/](https://www.aeris-data.fr/en/landing-page/?uuid=72b08c4b-cf05-4bd7-ae16-4c0dd2a889c3)  
767 [?uuid=72b08c4b-cf05-4bd7-ae16-4c0dd2a889c3](https://www.aeris-data.fr/en/landing-page/?uuid=72b08c4b-cf05-4bd7-ae16-4c0dd2a889c3) doi: 10.25326/42
- 768 Clarisse, L. (2019). *MetOp-C IASI Level 2 Sulphur Dioxide Total Column and Altitude.*  
769 *V2.1.0* [Dataset]. Retrieved from [https://www.aeris-data.fr/en/landing-page/](https://www.aeris-data.fr/en/landing-page/?uuid=3e81c051-cc66-4a81-a5e5-48cedcd53dfb)  
770 [?uuid=3e81c051-cc66-4a81-a5e5-48cedcd53dfb](https://www.aeris-data.fr/en/landing-page/?uuid=3e81c051-cc66-4a81-a5e5-48cedcd53dfb) doi: 10.25326/43
- 771 Clarisse, L., Coheur, P.-F., Theys, N., Hurtmans, D., & Clerbaux, C. (2014). The 2011  
772 Nabro eruption, a SO<sub>2</sub> plume height analysis using IASI measurements. *Atmos.*  
773 *Chem. Phys.*, 14(6), 3095–3111.
- 774 Coy, L., Newman, P., Wargan, K., Partyka, G., Strahan, S., & Pawson, S. (2022). Strato-

- 775 spheric Circulation Changes Associated with the Hunga Tonga-Hunga Ha’apai  
776 Eruption. *Geophysical Research Letters*, e2022GL100982.
- 777 Deshler, T. (2008). A review of global stratospheric aerosol: Measurements, importance,  
778 life cycle, and local stratospheric aerosol. *Atmospheric Research*, 90(2-4), 223–232.
- 779 Dhomse, S., Emmerson, K., Mann, G., Bellouin, N., Carslaw, K., Chipperfield, M., ...  
780 others (2014). Aerosol microphysics simulations of the Mt. Pinatubo eruption with  
781 the UM-UKCA composition-climate model. *Atmospheric Chemistry and Physics*,  
782 14(20), 11221–11246.
- 783 Dubovik, O., Holben, B., Eck, T. F., Smirnov, A., Kaufman, Y. J., King, M. D., ...  
784 Slutsker, I. (2002). Variability of absorption and optical properties of key aerosol  
785 types observed in worldwide locations. *Journal of the Atmospheric Sciences*, 59(3),  
786 590–608.
- 787 Dubovik, O., & King, M. D. (2000). A flexible inversion algorithm for retrieval of aerosol  
788 optical properties from sun and sky radiance measurements. *Journal of Geophysical  
789 Research: Atmospheres*, 105(D16), 20673–20696.
- 790 Dubovik, O., Sinyuk, A., Lapyonok, T., Holben, B. N., Mishchenko, M., Yang, P., ...  
791 Slutsker, I. (2006). Application of spheroid models to account for aerosol par-  
792 ticle nonsphericity in remote sensing of desert dust. *J. Geophys. Res. Atm.*,  
793 111(D11208).
- 794 Dubovik, O., Smirnov, A., Holben, B., King, M., Kaufman, Y., Eck, T., & Slutsker, I.  
795 (2000). Accuracy assessments of aerosol optical properties retrieved from Aerosol  
796 Robotic Network (AERONET) Sun and sky radiance measurements. *Journal of  
797 Geophysical Research: Atmospheres*, 105(D8), 9791–9806.
- 798 Duchamp, C., Wrana, F., Legras, B., Sellitto, P., Belhadji, R., & von Savigny, C. (2023).  
799 Observation of the aerosol plume from the 2022 Hunga Tonga-Hunga Ha’apai  
800 eruption with SAGE III/ISS. *Authorea Preprints*. Retrieved August 2023,  
801 from <https://www.doi.org/10.22541/essoar.168771425.59096731/v1> doi:  
802 10.22541/essoar.168771425.59096731/v1
- 803 Eck, T., Holben, B., Reid, J., Dubovik, O., Smirnov, A., O’neill, N., ... Kinne, S. (1999).  
804 Wavelength dependence of the optical depth of biomass burning, urban, and desert  
805 dust aerosols. *Journal of Geophysical Research: Atmospheres*, 104(D24), 31333–  
806 31349.
- 807 Eck, T. F., Holben, B. N., Sinyuk, A., Pinker, R., Goloub, P., Chen, H., ... others  
808 (2010). Climatological aspects of the optical properties of fine/coarse mode aerosol  
809 mixtures. *Journal of Geophysical Research: Atmospheres*, 115(D19).
- 810 ESA Copernicus. (2020). *Sentinel-5P TROPOMI Level 2 Sulphur Dioxide Total Column.  
811 Version 02*. [Dataset]. Retrieved from <https://scihub.copernicus.eu/> doi: 10  
812 .5270/S5P-74eidii
- 813 EUMETRAIN. (2023). *SEVIRI ash RGB Quick Guide*. Retrieved from [https://  
814 resources.eumetrain.org/rgb-quick-guides/index.html](https://resources.eumetrain.org/rgb-quick-guides/index.html)
- 815 EUMETSAT. (2018). *MetOp IASI Level 2 Sulphur Dioxide Total Column* [Dataset].  
816 Retrieved from [https://navigator.eumetsat.int/product/EO:EUM:DAT:METOP:  
817 MXI-N-SO2](https://navigator.eumetsat.int/product/EO:EUM:DAT:METOP:MXI-N-SO2)
- 818 EUMETSAT. (2023). *Compilation of RGB recipes*. Retrieved January 2023, from  
819 [https://eumetrain.org/sites/default/files/2022-10/RGB\\_recipes.pdf](https://eumetrain.org/sites/default/files/2022-10/RGB_recipes.pdf)
- 820 Folch, A., Costa, A., Durant, A., & Macedonio, G. (2010). A model for wet aggrega-  
821 tion of ash particles in volcanic plumes and clouds: 2. Model application. *Journal of  
822 Geophysical Research (Solid Earth)*, 115(B14), 9202. doi: 10.1029/2009JB007176
- 823 Foucart, B., Sellegri, K., Tulet, P., Rose, C., Metzger, J.-M., & Picard, D. (2018). High

- 824 occurrence of new particle formation events at the Maïdo high-altitude observatory  
825 (2150 m), Réunion (Indian Ocean). *Atmospheric Chemistry and Physics*, 18(13),  
826 9243–9261.
- 827 Giles, D. M., Sinyuk, A., Sorokin, M. G., Schafer, J. S., Smirnov, A., Slutsker, I., ...  
828 others (2019). Advancements in the Aerosol Robotic Network (AERONET) Ver-  
829 sion 3 database—automated near-real-time quality control algorithm with improved  
830 cloud screening for Sun photometer aerosol optical depth (AOD) measurements.  
831 *Atmospheric Measurement Techniques*, 12(1), 169–209.
- 832 Haywood, J. M., Jones, A., Clarisse, L., Bourassa, A., Barnes, J., Telford, P., ...  
833 Braesicke, P. (2010). Observations of the eruption of the Sarychev volcano and  
834 simulations using the HadGEM2 climate model. *J. Geophys. Res.*, 115, D21212.  
835 doi: 10.1029/2010JD014447
- 836 Hoffmann, A., Ritter, C., Stock, M., Maturilli, M., Eckhardt, S., Herber, A., & Neuber,  
837 R. (2010). Lidar measurements of the Kasatochi aerosol plume in August and  
838 September 2008 in Ny-Ålesund, Spitsbergen. *Journal of Geophysical Research:*  
839 *Atmospheres*, 115(D2).
- 840 Holben, B., Setzer, A., Eck, T., Pereira, A., & Slutsker, I. (1996). Effect of dry-season  
841 biomass burning on Amazon basin aerosol concentrations and optical properties,  
842 1992–1994. *Journal of Geophysical Research: Atmospheres*, 101(D14), 19465–  
843 19481.
- 844 Holben, B., Smirnov, A., Eck, T. F., Slutsker, I., Abuhassan, N., Newcomb, W. W., ...  
845 Lavenu, F. (2001). An emerging ground-based aerosol climatology- Aerosol optical  
846 depth from AERONET. *J. Geophys. Res.*, 106(D11), 12067–12097.
- 847 Holben, B. N., Eck, T., Slutsker, I., Smirnov, A., Sinyuk, A., Schafer, J., ... Dubovik, O.  
848 (2006). Aeronet’s version 2.0 quality assurance criteria. In *Remote sensing of the*  
849 *atmosphere and clouds* (Vol. 6408, pp. 134–147).
- 850 Holben, B. N., Eck, T. F., Slutsker, I., Tanré, D., Buis, J. P., Setzer, A., ... Smirnov,  
851 A. (1998). AERONET—A Federated Instrument Network and Data Archive for  
852 Aerosol Characterization. *Remote Sensing of Environment*, 66(1), 1 - 16. doi:  
853 10.1016/S0034-4257(98)00031-5
- 854 Japan Meteorological Agency. (2015). *Himawari 8, Advanced Himawari Imager (AHI),*  
855 *L1B* [Dataset]. Retrieved from [https://search.diasjp.net/en/dataset/](https://search.diasjp.net/en/dataset/Himawari_8.9)  
856 [Himawari\\_8.9](https://search.diasjp.net/en/dataset/Himawari_8.9)
- 857 Japan Meteorological Agency. (2023). *Himawari ash RGB quick guide*. Retrieved Jan-  
858 uary 2023, from [https://www.jma.go.jp/jma/jma-eng/satellite/VLab/QG/](https://www.jma.go.jp/jma/jma-eng/satellite/VLab/QG/RGB_QG_Ash_en.pdf)  
859 [RGB\\_QG\\_Ash\\_en.pdf](https://www.jma.go.jp/jma/jma-eng/satellite/VLab/QG/RGB_QG_Ash_en.pdf)
- 860 Jégou, F., Berthet, G., Brogniez, C., Renard, J.-B., François, P., Haywood, J. M., ...  
861 Daugeron, D. (2013). Stratospheric aerosols from the Sarychev volcano eruption  
862 in the 2009 Arctic summer. *Atmospheric Chemistry and Physics*, 13(13), 6533–  
863 6552. Retrieved from <http://www.atmos-chem-phys.net/13/6533/2013/> doi:  
864 10.5194/acp-13-6533-2013
- 865 Jenkins, S., Smith, C., Allen, M., & Grainger, R. (2023). Tonga eruption increases chance  
866 of temporary surface temperature anomaly above 1.5° c. *Nature Climate Change*,  
867 1–3.
- 868 Khaykin, S., Podglajen, A., Ploeger, F., Groß, J.-U., Tencé, F., Bekki, S., ... others  
869 (2022). Global perturbation of stratospheric water and aerosol burden by Hunga  
870 eruption. *Communications Earth & Environment*, 3(1), 316.
- 871 Kloss, C., Sellitto, P., Renard, J.-B., Baron, A., Bègue, N., Legras, B., ... others  
872 (2022). Aerosol characterization of the stratospheric plume from the volcanic

- 873 eruption at Hunga Tonga 15 January 2022. *Geophysical Research Letters*, 49(16),  
874 e2022GL099394.
- 875 Koren, I., Dagan, G., & Altaratz, O. (2014). From aerosol-limited to invigoration of  
876 warm convective clouds. *science*, 344(6188), 1143–1146.
- 877 Kravitz, B., Robock, A., Bourassa, A., Deshler, T., Wu, D., Mattis, I., ... others (2011).  
878 Simulation and observations of stratospheric aerosols from the 2009 Sarychev vol-  
879 canic eruption. *Journal of Geophysical Research: Atmospheres*, 116(D18).
- 880 Kremser, S., Thomason, L. W., von Hobe, M., Hermann, M., Deshler, T., Timmreck, C.,  
881 ... others (2016). Stratospheric aerosol—observations, processes, and impact on  
882 climate. *Reviews of Geophysics*, 54(2), 278–335.
- 883 Lac, C., Le Pichon, A., Listowski, C., Abbassi, G., Astafyeva, E., Baron, A., ... others  
884 (2022). *The eruption of the Hunga Tonga - Hunga Ha'apai volcano on January*  
885 *15, 2022: a shock of the Earth on a global scale* (Tech. Rep.). Groupe Thématique  
886 Atmosphère d'ALLENVI. Retrieved Jan 2023, from [https://zenodo.org/record/](https://zenodo.org/record/7678770/files/Tonga_FR_FINALE_DOI_v1.1.1.pdf)  
887 [7678770/files/Tonga\\_FR\\_FINALE\\_DOI\\_v1.1.1.pdf](https://zenodo.org/record/7678770/files/Tonga_FR_FINALE_DOI_v1.1.1.pdf) doi: 10.5281/zenodo.7678770
- 888 Legras, B., Duchamp, C., Sellitto, P., Podglajen, A., Carboni, E., Siddans, R., ...  
889 Ploeger, F. (2022). The evolution and dynamics of the Hunga Tonga–Hunga  
890 Ha'apai sulfate aerosol plume in the stratosphere. *Atmospheric Chemistry and*  
891 *Physics*, 22(22), 14957–14970.
- 892 Lurton, T., Jégou, F., Berthet, G., Renard, J.-B., Clarisse, L., Schmidt, A., ... Roberts,  
893 T. J. (2018). Model simulations of the chemical and aerosol microphysical evo-  
894 lution of the Sarychev Peak 2009 eruption cloud compared to in situ and satellite  
895 observations. *Atmospheric Chemistry and Physics*, 18(5), 3223–3247.
- 896 Mann, G., Dhomse, S., Deshler, T., Timmreck, C., Schmidt, A., Neely, R., & Thomason,  
897 L. (2015). Evolving particle size is the key to improved volcanic forcings. *Past*  
898 *Global Changes Magazine*, 23, 52–53.
- 899 Marshall, L. R., Maters, E. C., Schmidt, A., Timmreck, C., Robock, A., & Toohy, M.  
900 (2022). Volcanic effects on climate: recent advances and future avenues. *Bulletin of*  
901 *Volcanology*, 84(5), 1–14.
- 902 McCormick, M. P., Thomason, L. W., & Trepte, C. R. (1995). Atmospheric effects of the  
903 Mt Pinatubo eruption. *Nature*, 373, 399–404. doi: 10.1038/373399a0
- 904 Millan, L., Santee, M. L., Lambert, A., Livesey, N. J., Werner, F., Schwartz, M. J., ...  
905 others (2022). The Hunga Tonga–Hunga Ha'apai Hydration of the Stratosphere.  
906 *Geophysical Research Letters*, 49(13), e2022GL099381.
- 907 NASA/CNES/LARC/SD/ASDC. (2022). *CALIPSO Lidar Level 1B profile data, V4.51*  
908 [Dataset]. doi: 10.5067/CALIOP/CALIPSO/CAL\_LID\_L1-Standard-V4-51
- 909 O'Neill, N., Eck, T., Smirnov, A., Holben, B., & Thulasiraman, S. (2003). Spectral  
910 discrimination of coarse and fine mode optical depth. *J. Geophys. Res. Atmos.*,  
911 108(D17).
- 912 O'Neill, N. T., Perro, C., Saha, A., Lesins, G., Duck, T. J., Eloranta, E. W., ... others  
913 (2012). Properties of Sarychev sulphate aerosols over the Arctic. *J. Geophys. Res.*,  
914 117(D4).
- 915 Pinto, J. P., Turco, R. P., & Toon, O. B. (1989). Self-limiting physical and chemical  
916 effects in volcanic eruption clouds. *Journal of Geophysical Research: Atmospheres*,  
917 94(D8), 11165–11174.
- 918 Prata, A. (1989). Infrared radiative transfer calculations for volcanic ash clouds. *Geo-*  
919 *physical research letters*, 16(11), 1293–1296.
- 920 Proud, S. R., Prata, A. T., & Schmauß, S. (2022). The January 2022 eruption of Hunga  
921 Tonga–Hunga Ha'apai volcano reached the mesosphere. *Science*, 378(6619), 554–

- 922 557.
- 923 Randriambelo, T., Baray, J.-L., & Baldy, S. (2000). Effect of biomass burning, convec-
- 924 tive venting, and transport on tropospheric ozone over the Indian Ocean: Reunion
- 925 island field observations. *Journal of Geophysical Research: Atmospheres*, *105*(D9),
- 926 11813–11832.
- 927 Ridley, D., Solomon, S., Barnes, J., Burlakov, V., Deshler, T., Dolgii, S., . . . Vernier,
- 928 J. P. (2014). Total volcanic stratospheric aerosol optical depths and implications for
- 929 global climate change. *Geophysical Research Letters*, *41*, 7763–7769.
- 930 Robock, A. (2000). Volcanic eruptions and climate. *Reviews of Geophysics*, *38*, 191–220.
- 931 doi: 10.1029/1998RG000054
- 932 Russell, P., Livingston, J., Pueschel, R., Bauman, J., Pollack, J., Brooks, S., . . .
- 933 Bergstrom, R. (1996). Global to microscale evolution of the Pinatubo volcanic
- 934 aerosol derived from diverse measurements and analyses. *J. Geophys. Res. D.*,
- 935 *101*(13), 18.
- 936 Schoeberl, M., Wang, Y., Ueyama, R., Taha, G., Jensen, E., & Yu, W. (2022). Analysis
- 937 and Impact of the Hunga Tonga-Hunga Ha’apai Stratospheric Water Vapor Plume.
- 938 *Geophysical Research Letters*, *49*(20), e2022GL100248.
- 939 Seinfeld, J., & Pandis, S. N. (2012). *Atmospheric chemistry and physics: from air pollu-*
- 940 *tion to climate change*. New Jersey, USA: John Wiley and Sons.
- 941 Sellitto, P., Podglajen, A., Belhadji, R., Boichu, M., Carboni, E., Cuesta, J., . . . others
- 942 (2022). The unexpected radiative impact of the Hunga Tonga eruption of 15th
- 943 January 2022. *Communications Earth & Environment*, *3*(1), 1–10.
- 944 Sinyuk, A., Holben, B. N., Eck, T. F., Giles, D. M., Slutsker, I., Korokin, S., . . . Lya-
- 945 pustin, A. (2020). The AERONET Version 3 aerosol retrieval algorithm, associated
- 946 uncertainties and comparisons to Version 2. *Atmospheric Measurement Techniques*
- 947 *Discussions*, *12*, 1–80.
- 948 Sioris, C., Boone, C., Bernath, P., Zou, J., McElroy, C., & McLinden, C. (2010). Atmo-
- 949 spheric chemistry experiment (ace) observations of aerosol in the upper troposphere
- 950 and lower stratosphere from the Kasatochi volcanic eruption. *Journal of Geophysical*
- 951 *Research: Atmospheres*, *115*(D2).
- 952 Solomon, S. (1999). Stratospheric ozone depletion: A review of concepts and history. *Re-*
- 953 *views of Geophysics*, *37*(3), 275–316.
- 954 Stothers, R. B. (2001). A chronology of annual mean effective radii of stratospheric
- 955 aerosols from volcanic eruptions during the twentieth century as derived from
- 956 ground-based spectral extinction measurements. *Journal of Geophysical Research:*
- 957 *Atmospheres*, *106*(D23), 32043–32049.
- 958 Taha, G., Loughman, R., Colarco, P., Zhu, T., Thomason, L., & Jaross, G. (2022).
- 959 Tracking the 2022 Hunga Tonga-Hunga Ha’apai Aerosol Cloud in the Upper and
- 960 Middle Stratosphere Using Space-Based Observations. *Geophysical Research Let-*
- 961 *ters*, *49*(19), e2022GL100091.
- 962 Taha, G., Loughman, R., Zhu, T., Thomason, L., Kar, J., Rieger, L., & Bourassa, A.
- 963 (2021). OMPS LP Version 2.0 multi-wavelength aerosol extinction coefficient re-
- 964 trieval algorithm. *Atmospheric Measurement Techniques*, *14*(2), 1015–1036.
- 965 Tanré, D., Kaufman, Y., Holben, B. e. a., Chatenet, B., Karnieli, A., Lavenue, F., . . .
- 966 Smirnov, A. (2001). Climatology of dust aerosol size distribution and optical
- 967 properties derived from remotely sensed data in the solar spectrum. *Journal of*
- 968 *Geophysical Research: Atmospheres*, *106*(D16), 18205–18217.
- 969 Textor, C., Graf, H. F., Herzog, M., Oberhuber, J. M., Rose, W. I., & Ernst, G. G. J.
- 970 (2006). Volcanic particle aggregation in explosive eruption columns. Part II:

- 971 Numerical experiments. *Journal of Volcanology and Geothermal Research*, 150,  
972 378–394. doi: 10.1016/j.jvolgeores.2005.09.008
- 973 Theys, N., De Smedt, I., Yu, H., Danckaert, T., van Gent, J., Hörmann, C., ... others  
974 (2017). Sulfur dioxide retrievals from TROPOMI onboard Sentinel-5 Precursor:  
975 algorithm theoretical basis. *Atmospheric Measurement Techniques*, 10(1), 119–153.
- 976 Theys, N., Hedelt, P., De Smedt, I., Lerot, C., Yu, H., Vlietinck, J., ... others (2019).  
977 Global monitoring of volcanic SO<sub>2</sub> degassing with unprecedented resolution from  
978 TROPOMI onboard Sentinel-5 Precursor. *Scientific reports*, 9(1), 1–10.
- 979 Thomason, L. W., Kovilakam, M., Schmidt, A., Von Savigny, C., Knepp, T., & Rieger, L.  
980 (2021). Evidence for the predictability of changes in the stratospheric aerosol size  
981 following volcanic eruptions of diverse magnitudes using space-based instruments.  
982 *Atmospheric Chemistry and Physics*, 21(2), 1143–1158.
- 983 Tilmes, S., Müller, R., & Salawitch, R. (2008). The sensitivity of polar ozone depletion to  
984 proposed geoengineering schemes. *Science*, 320(5880), 1201–1204.
- 985 Timmreck, C., Graf, H.-F., Lorenz, S. J., Niemeier, U., Zanchettin, D., Matei, D., ...  
986 Crowley, T. J. (2010). Aerosol size confines climate response to volcanic super-  
987 eruptions. *Geophysical Research Letters*, 37(24).
- 988 Timmreck, C., Lorenz, S. J., Crowley, T. J., Kinne, S., Raddatz, T. J., Thomas, M. A., &  
989 Jungclaus, J. H. (2009). Limited temperature response to the very large AD 1258  
990 volcanic eruption. *Geophysical Research Letters*, 36(21).
- 991 Torres, B., Dubovik, O., Toledano, C., Berjón, A., Cachorro, V. E., Lapyonok, T., ...  
992 Goloub, P. (2014). Sensitivity of aerosol retrieval to geometrical configuration  
993 of ground-based sun/sky radiometer observations. *Atmospheric Chemistry and*  
994 *Physics*, 14(2), 847–875.
- 995 Vernier, J.-P., Timmreck, C., & Kremser, S. (2022). *Atmospheric impacts of the 2022*  
996 *Hunga Tonga-Hunga Ha’apai (HT-HH) eruption* (Tech. Rep.). SPARC SSiRC com-  
997 munity. Retrieved from [www.sparc-ssirc.org/downloads/VolRes\\_summary\\_of\\_the](http://www.sparc-ssirc.org/downloads/VolRes_summary_of_the_Hunga-Vfinal.pdf)  
998 [\\_Hunga-Vfinal.pdf](http://www.sparc-ssirc.org/downloads/VolRes_summary_of_the_Hunga-Vfinal.pdf)
- 999 Vömel, H., Evan, S., & Tully, M. (2022). Water vapor injection into the stratosphere by  
1000 Hunga Tonga-Hunga Ha’apai. *Science*, 377(6613), 1444–1447.
- 1001 Wang, X., Randel, W., Zhu, Y., Tilmes, S., Starr, J., Yu, W., ... others (2022). Strato-  
1002 spheric climate anomalies and ozone loss caused by the Hunga Tonga volcanic  
1003 eruption. *Authorea Preprints*. Retrieved from [https://www.authorea.com/doi/](https://www.authorea.com/doi/full/10.1002/essoar.10512922.1)  
1004 [full/10.1002/essoar.10512922.1](https://www.authorea.com/doi/full/10.1002/essoar.10512922.1) doi: 10.1002/essoar.10512922.1
- 1005 Winker, D. M., Vaughan, M. A., Omar, A., Hu, Y., Powell, K. A., Liu, Z., ... Young,  
1006 S. A. (2009). Overview of the CALIPSO mission and CALIOP data processing  
1007 algorithms. *Journal of Atmospheric and Oceanic Technology*, 26(11), 2310–2323.
- 1008 Wrana, F., Von Savigny, C., Zalach, J., & Thomason, L. W. (2021). Retrieval of strato-  
1009 spheric aerosol size distribution parameters using satellite solar occultation mea-  
1010 surements at three wavelengths. *Atmospheric Measurement Techniques*, 14(3),  
1011 2345–2357.
- 1012 Zhu, Y., Bardeen, C. G., Tilmes, S., Mills, M. J., Wang, X., Harvey, V. L., ... others  
1013 (2022). Perturbations in stratospheric aerosol evolution due to the water-rich plume  
1014 of the 2022 Hunga-Tonga eruption. *Communications Earth & Environment*, 3(1),  
1015 1–7.